

37 diatexites, supporting new nucleation of zircon in migmatites.

38 In the Ryoke metamorphic belt at the Aoyama area, monazite from migmatites records the
39 prograde growth age of 96.5 ± 1.9 Ma. Using the difference of growth timing of monazite and zircon,
40 the duration of metamorphism higher than the amphibolite facies grade is estimated to be ca. 6 Myr.

41

42 Keywords: zircon, migmatite, melt inclusion, glass, crystal size distribution, duration of
43 metamorphism.

44

45

Introduction

46

47 Behavior of zircon during the metamorphism is a matter of great interest because zircon could
48 grow during many stages of metamorphism and the U-Pb spot ages of this mineral could constrain
49 the timing of its growth due to the sluggish nature of the Pb diffusion in it (e.g. Harley et al. 2007;
50 Rubatto and Hermann 2007). Microstructural information gives significant constraints on the origin
51 of zircon (Vavra et al. 1996; 1999; Schaltegger et al. 1999; Corfu et al. 2003; Geisler et al. 2007;
52 Rubatto and Hermann 2007; Higashino et al. 2012), so understanding the mechanism of
53 microstructure formation is of great importance. Above all, behavior of zircon at the amphibolite to
54 granulite facies transition is important since the role of partial melting on the growth and
55 microstructure formation of zircon can be understood from such studies (e.g. Schiøtte et al. 1989;
56 Vavra et al. 1999; Bowman et al. 2011). In the polymetamorphic orthogneiss from northern Labrador,
57 Canada, almost no zircon grows in the amphibolite facies gneisses, and it starts to grow near the
58 amphibolite-granulite facies transition (Schiøtte et al. 1989). Vavra et al. (1999) described the zoning
59 pattern of zircon from the amphibolite-granulite facies transition of the Ivrea Zone (Southern Alps)
60 in detail. In the Ivrea Zone, this grade of metasediments accompanies partial melting, and all the
61 zircon overgrowth was supposed to have formed entirely in an anatectic environment. They observed
62 an angular shape of inherited core of zircon in metasediments and interpreted that it is not affected
63 by the partial dissolution process. Since dust-like tiny zircons are abundant in the metasediments,
64 they assumed the Ostwald ripening as a possible growth mechanism of zircon overgrowth, and
65 considered that such a process took place during the prograde metamorphism. They recognized three
66 patterns of zircon overgrowth based on morphology and internal structure as follows; (i) prismatic
67 (prism-blocked) with low Th/U ratio and dark-cathodoluminescence (dark-CL), (ii) stubby with
68 medium Th/U ratio, and (iii) isometric with high Th/U ratio and bright-CL. The former two were
69 observed at amphibolite facies and the latter two was observed at granulite facies. They ascribed
70 prismatic zoning to be due to the growth in amphibolite facies H₂O saturated melt whereas isometric
71 zoning to be due to the growth in granulite facies H₂O undersaturated melt (Vavra et al. 1999).

72 Recently, melt inclusions are found in migmatites and granulites (Cesare et al. 2003; 2009; 2011).

73 One of the important host minerals of the melt inclusions is zircon (Cesare et al. 2003). The melt
74 inclusions are the direct evidence of the partial melting, and thus they enable to reliably constrain the
75 timing and environment in which zircon grew. Cesare et al. (2009) reports a garnet porphyroblast
76 that includes a monazite with melt inclusion and a zircon with an euhedral overgrowth. They
77 interpret that zircon growth in an anatectic environment was almost simultaneous with the garnet
78 growth, and occurred early in the melting process (Cesare et al. 2009). However, systematic
79 evaluation of zircon microstructure formed under the amphibolite to granulite facies metamorphism
80 that utilizes melt inclusions to constrain the timing of zircon microstructure formation is not
81 sufficiently available yet.

82 In this study, zircon in the upper-amphibolite to granulite facies pelitic and psammitic
83 metamorphic rocks of the Ryoke metamorphic belt at the Aoyama area are studied in detail in order
84 to understand the behavior of zircon in the anatectic migmatite front. The presence of melt inclusions
85 in the zircon rims, resorption microstructure of near-peak overgrowth truncated by the later
86 overgrowth, and the result of laser ablation inductively coupled plasma mass spectrometry
87 (LA-ICP-MS) U-Pb dating of zircon in combination with X-ray fluorescence (XRF) and modal
88 analyses show that the zircon rims of the Aoyama area partly grew during the near-peak
89 metamorphism in the presence of melt, and after partial resorption, further overgrowth developed
90 during the retrograde, melt crystallization stage.

91 Mineral abbreviations are after Kretz (1983).

92

93 **Geological outline of the Aoyama area**

94

95 The Ryoke metamorphic belt shows an elongated distribution over 800 km in SW Japan (Fig. 1a),
96 and is one of the most famous high-temperature, low-pressure type metamorphic belts in the world
97 (Miyashiro 1965; Okudaira et al. 1993; Okudaira 1996; Ikeda 1998a, b; Brown 1998; Nakajima
98 1994; Suzuki and Adachi 1998; Kawakami and Ikeda 2003; Kawakami 2004). It is mainly composed
99 of pelitic and psammitic metamorphic rocks and metacherts, and the highest grade zones are
100 considered to have reached granulite facies conditions at the metamorphic peak (e.g. Ikeda 2002).
101 The metamorphic belt grades into the unmetamorphosed sedimentary complex of the Mino-Tanba
102 terrane to the north that is mainly made up of Middle to Late Jurassic turbidites and shales (e.g.,
103 Wakita 1987).

104 The Aoyama area is one of the well-studied areas in the Ryoke metamorphic belt, where
105 high-grade metasedimentary rocks are widely exposed (Yoshizawa et al. 1966; Hayama et al. 1982;
106 Takahashi and Nishioka 1994; Kawakami 2001a; Kawakami and Nishioka 2012) (Fig. 1b). The rock
107 facies of the pelitic-psammitic rocks are the schists in the northern half of the area (white part of Fig.
108 1b), and are anatectic migmatites in the southern half of the area (gray part of Fig. 1b). Migmatites

109 are mostly metatexite, but diatexite is also common in the southwestern part of the migmatite
110 dominant zone. The chemical Th–U–total Pb isochron method (CHIME) dating of monazite from the
111 migmatites records the prograde monazite growth age of 96.5 ± 1.9 Ma during the regional, Ryoke
112 metamorphism (Kawakami and Suzuki 2011). This is similar to the CHIME monazite age of the
113 Ryoke metamorphic rocks reported from other areas where contact metamorphism by granite
114 intrusion is not significant (e.g. Suzuki and Adachi 1998).

115 The Kabuto granodiorite and the Ao granite that postdate regional metamorphism intrude
116 discordantly to the foliations of metamorphic rocks in the Aoyama area (Yoshida et al. 1995). The
117 Kabuto granodiorite gives the Rb–Sr–whole-rock age of 79.2 ± 10.2 Ma (Tainosho et al. 1999) and
118 accompanies a contact aureole. The Ao granite gives the CHIME monazite age of 79.8 ± 3.9 Ma
119 (Kawakami and Suzuki 2011). Monazite from the migmatite zone widely records 83.5 ± 2.4 Ma
120 thermal event in addition to the 96.5 ± 1.9 Ma age (Kawakami and Suzuki 2011) although the
121 contact aureole is not evident from the major metamorphic mineral assemblage (Takahashi and
122 Nishioka 1994). Kawakami and Suzuki (2011) attributed 83.5 ± 2.4 Ma overprint to the thermal
123 effect and monazite–fluid interaction caused by the intrusion of the Ao granite and the Kabuto
124 granodiorite.

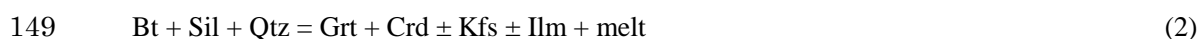
125 The Aoyama area is previously divided into two regional metamorphic zones and one contact
126 metamorphic zone, utilizing mineral assemblages in pelitic lithology (Kawakami 2001a). The
127 regional metamorphic zones in the order of increasing metamorphic grade are (i) Sil–Kfs zone,
128 where Ms + Qtz is unstable and Sil + Kfs + Bt is stable, and (ii) Grt–Crd zone, where Grt + Crd + Bt
129 ± Sil is stable. The contact metamorphic zone is recognized by the occurrence of Grt + Crd
130 assemblage in the granodiorite side (Fig. 1b). The peak pressure–temperature (*P–T*) conditions are
131 estimated to be 3.0–4.0 kbar, 615–670 °C for the Sil–Kfs zone, and 4.5–6.0 kbar, 650–800 °C for the
132 Grt–Crd zone (Kawakami 2001a). These estimates are based on the Grt–Bt geothermometers and
133 GASP geobarometers, possibly giving the lowest temperature estimates due to the retrograde
134 re-equilibrium between garnet and biotite. High spessartine content in the garnet from the
135 schist-dominant part of the Grt–Crd zone suggests that introduction of MnO into garnet stabilized the
136 Grt + Crd assemblage even under the lower temperature condition than the petrogenetic grid for the
137 KFMASH system predicts (Kawakami, 2001b). A pseudosection of Wei et al. (2004) constructed for
138 KMnFMASH + quartz system using typical pelite composition ($M_{Mn} = Mn/(Mn+Fe+Mg) = 0.007$)
139 of Mahar et al. (1997) shows that increase of M_{Mn} widens the stability field of Grt + Crd assemblage
140 very much. With $M_{Mn} = 0.03$, it is stable in subsolidus field even at 2 kbar, 650 °C. This is consistent
141 with the whole-rock Mn content of pelitic metamorphic rocks in the Aoyama area having a M_{Mn}
142 value up to 0.03 (Kawakami 2001b) and with the field observation that Grt + Crd assemblage is
143 found not only in migmatite-dominant area but also in the schist-dominant area. Therefore, effect of
144 Mn is probably responsible for the low-temperature estimates for the Grt + Crd bearing samples in

145 the Aoyama area.

146 In the Grt-Crd zone, dehydration melting reaction such as



148 and



150 are responsible for the formation of migmatites (Kawakami 2001a, b).

151 Besides the Grt-Crd isograd that is subparallel to the schist/migmatite lithological boundary, a line
152 marking the breakdown of tourmaline was mapped and termed the ‘tourmaline-out isograd’
153 (Kawakami 2001a, 2004). This isograd is further extended to the western side of the Aoyama area in
154 the present study (Fig. 1b). Near this isograd, magmatic andalusite is locally found, based on which
155 nearly isothermal decompression *P-T* path was proposed for the Grt-Crd zone (Kawakami 2002).
156 Melt extraction of 12–14 wt.% from the migmatite zone is estimated in the Aoyama area (Kawakami
157 and Kobayashi 2006).

158

159 **Sample description and methodology**

160

161 Samples used in this study are from the Grt-Crd zone where lithological change from schist to
162 migmatite as a function of increasing metamorphic grade can be observed (Fig. 1b). Three pelitic
163 and psammitic schists, 13 metatexites and 4 diatexites were collected (Fig. 1b). Mineral assemblage
164 and other details of the samples used in this study are summarized in Table 1.

165 These samples were prepared as polished thin section for the electron microprobe analysis of
166 constituting minerals and modal analysis of zircon. Remaining halves of the rock chips used for thin
167 sectioning (i.e., the same area with a thin section, ca. 5 mm thickness) were powdered, and utilized
168 in the trace element analysis by the XRF spectrometer Rigaku 3070 (Goto and Tatsumi 1996) at the
169 Geothermal Research Institute, Kyoto University. The migmatite sample is chemically banded and
170 the distribution of zircon within a sample is heterogeneous to some extent. In order to minimize such
171 effect in comparing zircon mode and whole-rock Zr content, using ‘the same system size’ is
172 preferable. This is why the remaining halves of the rock chips used for thin sectioning were utilized
173 in the determination of whole-rock Zr concentration.

174 Zircon grains in the thin section were observed under the SEM-EDS (Hitachi S-3500H equipped
175 with EDAX X-ray analytical system) and JEOL JXA8105 superprobe using back scattered electron
176 (BSE) images, qualitative analysis and an X-ray imaging. Size of zircon (major and minor axes)
177 whose major axis is more than 20 μm (written as ‘zircon (> 20 μm)’ hereafter) was measured using
178 BSE image of WDS. Zircon (< 20 μm) was not counted nor measured because they are so common
179 and it is difficult not to overlook them. Using this grain size data of zircon (> 20 μm), crystal size
180 distributions (CSDs) were calculated and CSD plots were constructed for each sample, following

181 Cashman and Ferry (1988) and Morishita (1992). The number of zircon crystals per size class and
182 per unit volume (N_v) is represented by $N_v = (c/a)^{1.5} / \Delta L$ (Cashman and Ferry 1988; Moroshita 1992),
183 where c , a and ΔL are the number of zircon crystals within the size class, measured area (whole
184 thin section in this study), and the size class (5 μm in this study).

185 Modal amount of zircon (> 20 μm) was determined using the BSE images as follows:

186 Modal amount of zircon (> 20 μm)

187 = (Sum of the area of zircon (> 20 μm) in a thin section)/(area of whole thin section),

188 where area of each zircon grain was calculated in two ways; assuming ellipsoidal shape of zircon
189 grains or rectangular shape of them (Table 1). The latter gives the possible maximum modal amount
190 of zircon.

191 The X-ray elemental mapping of whole thin section was performed for the sample AN44, in order
192 to determine the CSD plot of zircon covering zircon (< 20 μm). The beam diameter was 3 μm and
193 the step for the mapping was 5 μm each. The grain size of zircon was determined using the elemental
194 map of Zr and ‘analyze particles’ function of the ImageJ software. Feret’s diameter of each grain
195 calculated by ImageJ software was used to determine the CSD of zircon. Comparison of this CSD
196 with the CSD data obtained by the modal counting of zircon enabled to convert the apparent grain
197 size obtained by the elemental mapping to the real grain size.

198 Zircon grains in selected schist and migmatite samples from the Grt-Crd zone (Table 1) were
199 utilized in U-Pb dating using a Nu AttoM single-collector ICP-MS coupled to a NWR-193
200 laser-ablation system utilizing a 193 nm ArF excimer laser at Kyoto University. The zircon dating
201 was performed *in situ* on polished thin sections after BSE and CL image observations. Instrumental
202 parameters are listed in Table 2. The laser was operated with output energy of ~ 4.4 mJ per pulse,
203 repetition rate of 6 Hz and laser spot size of 20 μm in diameter, providing an estimated power
204 density of the sample of 1.60-2.23 J/cm². The pulse count was 100 shots. The ablation occurs in He
205 gas within the sample cell, and then the ablated sample aerosol and He gas were mixed with Ar gas
206 downstream of the cell. He minimizes redistribution of ejecta or condensates while Ar provides
207 efficient sample transport to the ICP-MS (Eggins et al. 1998; Gunther and Heinrich 1999; Jackson et
208 al. 2004). The signal-smoothing device was applied to minimize the introduction of large aerosols
209 into the ICP, reducing signal spikes (Tunheng and Hirata 2004).

210 The ICP-MS is optimized using continuous ablation of a 91500 zircon standard (Wiedenbeck et al.
211 1995; 2004) and NIST SRM 610 to provide maximum sensitivity. Data were acquired on seven
212 isotopes, ²⁰²Hg, ²⁰⁴Pb, ²⁰⁶Pb, ²⁰⁷Pb, ²⁰⁸Pb, ²³²Th, and ²³⁸U using a peak jumping acquisition mode,
213 which measures the signal intensity at the peak top.

214 Background and ablation data for each analysis were collected over 150 and 11 seconds,
215 respectively. Backgrounds were measured with the laser shutter closed and employing identical
216 settings and gas flows to those used during ablation. Data were acquired consisting of multiple

217 groups of 10 sample unknowns bracketed by quartets of NIST SRM 610 and 91500 zircon standards
218 (Wiedenbeck et al, 1995; 2004), which are sandwiched by a background analysis.

219 ^{202}Hg was monitored to correct the isobaric interference of ^{204}Hg on ^{204}Pb . To reduce the isobaric
220 interference, an Hg-trap device with an activated charcoal filter was applied to the Ar make-up gas
221 before mixing with He carrier gas (Hirata et al. 2005). Prior to each individual analysis, regions of
222 interest were pre-ablated using a pulse of the laser with a spot size of 35 μm in diameter to remove
223 potential surface contamination, dramatically reducing common Pb contamination (Iizuka and Hirata
224 2004). The average 204 intensities of background and samples for all the analysis performed in this
225 study are 7680 cps and 7725 cps, respectively (average 204 intensity of selected analysis shown in
226 Table 3 is 7690 cps). Most of 204 intensity for background is Hg, as indicated by a background
227 $^{202}\text{Hg}/204$ ratio indistinguishable from natural Hg, $^{202}\text{Hg}/^{204}\text{Hg} = 29.863/6.865$. When ^{204}Pb data for
228 unknown sample was obtained and a sample has a discordant age without common Pb correction,
229 common Pb correction was applied to the sample following the two-stage model of Stacey and
230 Kramers (1975). The maximum level of the correction was fourth time. If the sample required more
231 than the maximum level of correction, the age of sample was discarded. The effect of the common
232 Pb correction was factored into the analytical errors on the ages.

233 All data reduction including the common Pb correction was conducted off-line using in-house
234 Excel spreadsheet. Background intensities were interpolated using an averaged value among four
235 background data acquired before and after the each unknown sample groups. The mean and standard
236 deviation of the measured ratios among each eight NIST SRM 610 and 91500 zircon standard data
237 bracketing unknown sample groups were calculated, and the mean and standard deviation measured
238 for 91500 zircon standard were applied for age estimate and uncertainty propagation. All
239 uncertainties are quoted at the 2 sigma level. ^{235}U was calculated from ^{238}U using a $^{238}\text{U}/^{235}\text{U}$ ratio of
240 137.88 (Jaffey et al. 1971).

241 Inclusions phases in zircon grains were observed using JEOL FE-SEM at Osaka University and
242 transmitted electron microscope (TEM) Hitachi H8000k equipped with KEVEX EDS system at
243 Kyoto University. The TEM samples were prepared from the polished thin sections using focused
244 ion beam (FIB) FEI Quanta 200 3DS at Kyoto University.

245

246

Results

247

248

Modal amount of zircon and whole-rock Zr concentration

249

250 The modal analysis of zircon ($> 20 \mu\text{m}$) was performed on 11 pelitic and psammitic schists,
251 metatexite and diatexite samples (Fig. 1b, Table 1). Figure 2 is a diagram showing the relationship
252 between the whole-rock Zr content and the modal amount of zircon ($> 20 \mu\text{m}$). Comparing the

253 modal amount of zircon (> 20 μm) in schists, metatexites and diatexites having almost the same
254 whole-rock Zr content around 170-190 ppm, there is a tendency that the modal amount of zircon (>
255 20 μm) is higher in the schists than the metatexites, and diatexites are in between them (Fig. 2).
256 About 60% of the whole-rock Zr is hosted in zircon (> 20 μm) in schists, but zircon (> 20 μm) hosts
257 less than 40% of whole-rock Zr in metatexites. In diatexites, 30-50% of the whole-rock Zr is hosted
258 in zircon (> 20 μm).

259 Figure 3 is a plot showing a grain size distribution of zircon determined by an X-ray elemental
260 mapping of a whole thin section of a metatexite sample AN44. Open diamonds are plotted using
261 Feret's diameter determined by the elemental mapping and the ImageJ software. This diameter could
262 be affected by step sizes and beam diameter of the elemental mapping. Grain size of the gray squares
263 was determined under BSE observation, and thus considered reliable. The major axis of zircon is
264 used as a grain size in this study. These two methods gave different, but almost parallel, linear least
265 squares fit lines (Fig. 3). Since these two should be identical, and subtraction of 8 μm from the grain
266 sizes determined by the elemental mapping (solid triangles in Fig. 3) results in good coincidence
267 between the two (solid and dotted lines), we consider that the grain size distribution of the sample
268 AN44 covering all the zircon size range could be approximately represented by the solid triangle
269 data (Fig. 3).

270 Figure 4 is the summary of CSD plots for 2 schist samples (Fig. 4a, b), 4 metatexites (Fig. 4c-f),
271 and 4 diatexites (Fig. 4g-k). There is a tendency that the CSD plots of the grain size range of 25-40
272 μm commonly define a linear trend. It is rarely curved at the smallest grain size range (20-35 μm) in
273 sample Y32A. Data for coarse-grained zircons in the plot (more than 40-50 μm size in most cases)
274 tend to be discordant with the least squares fit lines (e.g., Fig. 4a, e-f, i-j), possibly due to the small
275 grain numbers (1 to 3).

276

277

Zircon in diatexites of the Grt-Crd zone

278

279 Zircon in the garnet-free diatexites from the Grt-Crd zone, especially those containing abundant
280 coarse-grained zircon grains, clearly shows the core-rim microstructure; core is the inherited part
281 from the protolith showing various ages (Fig. 5) and the rim overgrowths develop on it. The core-rim
282 boundary can be commonly identified by the presence of characteristic thin, dark-CL (bright BSE)
283 annulus (Fig. 5a-l, o-r, w-x). Although the dark annulus itself cannot be dated because it is too thin,
284 ubiquitous occurrence of it at the immediate contact between inherited core and the rim regardless of
285 the variety of the inherited core ages (Fig. 5) suggests that the dark-CL annulus is contemporaneous
286 with the rim overgrowth, and formed during the latest metamorphic event, that is, the Ryoke
287 metamorphism. The dark-CL annulus commonly includes tiny, dark inclusions of less than several
288 microns in diameter (Fig. 5a-l, o-r, w-x). Such inclusions are abundant in pyramid faces where

289 overgrowth is thicker and probably faster (Fig. 5c-d, i-j). This microstructure resembles very much
290 with that observed in zircons from the El Hoyazo enclave (Cesare et al. 2003). In the case of El
291 Hoyazo, one of the tiny inclusions was confirmed to be a rhyolitic glass.

292 In order to confirm the presence of melt inclusions in our sample, tiny inclusions present in the
293 dark-CL annulus of zircon were prepared for the TEM observation utilizing FIB. Figure 6 shows the
294 bright and dark field images of the sample G6 and the electron diffraction patterns of the inclusions
295 in it. Judging from the diffuse, halo pattern of the electron diffraction images, inclusions 1, 3 and 5
296 are the glass, and inclusions 2 and 4 are the mixture of glass and crystal. The EDS analysis under
297 TEM and FE-SEM shows that inclusion 3 is a glass containing K, Al and Si, and inclusion 1 is a
298 Si-rich glass. The melt inclusions rarely have pores (inclusion 2 of Fig. 6) that resembles to the
299 'micro- to nano-porosities' (terminology after Cesare et al. 2011) reported from nanogranites.
300 Presence of pores and daughter crystals in the glass inclusions in zircon is also observed in plutonic
301 rocks (Thomas et al. 2003).

302 The core of the zircon is often oscillatory zoned both in CL and BSE images and such a zoning is
303 truncated by the rim overgrowth (Fig. 5a-b, e-f, k-l). The shape of the core (inside of the dark-CL
304 annulus) is often angular (Fig. 5a-b, i-j), as observed in the case of metapelites from the amphibolite
305 and granulite facies transition in Ivrea Zone (Vavra et al. 1999), but the rounded ones are also
306 present (Fig. 5o-r). The important characteristic of the dark-CL annulus in the garnet-free diatexite
307 zircon is that it varies in thickness and commonly truncated by the lighter-colored overgrowth (Fig.
308 5a-b, g-h, w-x).

309 Zircon grains without the inherited core are not uncommon in the matrix and the grain size is ca.
310 35 μm (Fig. 5m-n), both in garnet-free and garnet-bearing diatexites. They show rounded shape and
311 lack zoning, and show similar CL brightness with the bright-CL overgrowth developed at the coarse
312 zircon rim. They also lack the dark-CL annulus. Based on transmitted light microscope observation,
313 some of them are the rim of the coarse grained zircon. However, common occurrence of ca. 35 μm
314 grains with young ages as reported below supports that some of them are newly nucleated ones
315 contemporaneous with the coarse-grained zircon rims.

316 Zircon with dark-CL annulus and tiny inclusion alignments are also found in the matrix and as
317 inclusions in garnet from the garnet-bearing diatexite. In a garnet-bearing diatexite sample G11,
318 major axis of zircon ($> 20 \mu\text{m}$) is mostly 20-30 μm (Fig. 4h) and the dark-CL annulus and tiny
319 inclusion alignments are rarely observed in the matrix zircon (Fig. 5o-p, s-x). Zircon inclusion in
320 garnet often has a major axis less than 30 μm (Fig. 5q-r), and has dark-CL annulus and tiny inclusion
321 alignment. Most of the matrix zircon lacks apparent inherited core, and their microstructure and
322 CL-intensity resemble to the possible newly nucleated grains observed in the garnet-free diatexites
323 (Fig. 5m-n). Some matrix zircon grains show dark-CL annulus truncated by the overgrowth rim (Fig.
324 5w-x) as in the case of garnet-free diatexites. Although it is still not clear whether this

325 microstructural difference between garnet-free and garnet-bearing diatexites are common in other
326 diatexites in the Aoyama area or not, the important observation in this study is that both zircon rim
327 overgrowth and newly crystallized grains can be recognized in garnet-free and garnet-bearing
328 diatexites, and zircon in these diatexites also share the characteristic that dark-CL annulus is further
329 truncated by the overgrown rim.

330 The LA-ICP-MS U-Pb dating of zircon rims and the grains without inherited cores give the
331 concordia age of ca. 90.3 ± 2.2 Ma (Fig. 7b). The cores give concordant ages of ca. 2100-1700 Ma,
332 ca. 550 Ma and ca. 250-120 Ma, and these are considered to be inherited, detrital ages (Fig. 7a).
333 Most of the rim overgrowths were too thin for the LA-ICP-MS U-Pb dating with 20 μm spot-size, so
334 that many mixed analyses of inherited core and rim resulted in the formation of discordia in the
335 concordia diagram (Fig. 7a). The Th/U ratio of the zircon core varies while that of the 90.3 ± 2.2 Ma
336 rim is very low, mostly below 0.02 (Table 3).

337

338

Zircon in schists and metatexites of the Grt-Crd zone

339

340 Zircon in pelitic and psammitic schist of the Grt-Crd zone is found in the matrix, and intimate
341 microstructural correlation between other mineral such as biotite is not observed. Microstructure of
342 zircon does not differ between the pelitic and psammitic lithology, and the dark-CL annulus
343 developed on the inherited core, accompanied by the inclusions similar to diatexite zircons, is rarely
344 observed (Fig. 8). Rim overgrowth, if present, is about several microns in thickness (Fig. 8c-h, k-l,
345 o-v). Zircon grains that do not have rim overgrowth are also common (Fig. 8a-b, m-n). Even in such
346 cases, inclusion alignments are found along the healed cracks that can be observed in CL images
347 (Fig. 8k-l). Shape of the core is often angular (Fig. 8e-h, k-l, q-r, u-v), although rounded variety is
348 also present.

349 Zircon in metatexite is found in the matrix (Fig. 9e-h, k-t), as well as inclusions in garnet
350 porphyroblasts (Fig. 9a-b, i-j) or biotite (Fig. 9m-n). Zircon in the matrix is commonly found
351 adjacent to biotite or quartz in mesosome and melanosome. It is rare in leucosome. The dark-CL
352 annulus with inclusions is developed in most of the zircon grains found in the matrix (Fig. 9e-h, k-t).
353 Nanogranite-like polyphase inclusion is included in the dark-CL annulus of zircon grain AN07a-7
354 (Fig. 9o-p). The dark-CL annulus is further overgrown by the brighter-CL overgrowth (Fig. 9e-h, k-t).
355 The thickness of the rim overgrowth is, in most cases, less than 10 μm . Shape of the core is often
356 angular (Fig. 9e-f, k-l, q-r), even if the zircon is included in garnet (Fig. 9i-j), although rounded
357 variety is also common (Fig. 9m-n).

358 Zircon inclusions in garnet porphyroblast are often less than 20 μm , with or without core-rim
359 microstructure (Fig. 9a-b, i-j). Monazite is also included in the same garnet, so monazite and zircon
360 coexisted during the near-peak metamorphism when garnet grew. An example of inclusion zircon

361 from sample AN07 has angular-shaped core, overgrown by the dark-CL annulus and brighter-CL
362 overgrowth on it (Fig. 9i-j). Dark-CL annulus has many inclusions of unidentified phases less than
363 several microns in diameter (Fig. 9i-j, shown by arrows), microstructure of which resembles very
364 much to the zircon with melt inclusions found in diatexites (Fig. 5). Different from diatexites, the
365 dark-CL annulus is not truncated by the brighter-CL overgrowths in most of the metatexite samples
366 (Fig. 9).

367 The dark-CL annulus and brighter-CL overgrowth on zircon in schists and metatexites are thinner
368 than the spot size (20 μm) of the LA-ICP-MS U-Pb dating. Because of this, most dating on the
369 zircon rim could be only done as mixtures with the inherited core. The result is plotted on a
370 concordia diagram (Fig. 10). Most results are lying on a discordia, which is actually a mixing line
371 resulted from the mixed analysis of the core and rim. The inferred lower intercept around ca. 90 Ma
372 implies the presence of the rim overgrowth of ca. 90 Ma (Fig. 10). A zircon grain from the
373 metatexite (sample AN52) with characteristic core-rim microstructure gave near-concordant age of
374 115 ± 6.0 Ma and relatively low Th/U ratio of 0.16 (Fig. 9g-h). Presence of this kind of mixed age
375 also supports the growth of young zircon rim in metatexites. Therefore, the thin zircon rim observed
376 in the schists and metatexites is probably identical to the 90.3 ± 2.2 Ma zircon rim observed in
377 diatexites. The cores of zircon from schists and metatexites give concordant U-Pb ages of ca. 2500
378 Ma, ca. 2200-1700 Ma, ca. 600 Ma and ca. 230-120 Ma, and these are considered to be inherited,
379 detrital ages (Fig. 10).

380

381 **Discussion**

382

383 **Behavior of zircon at the schist-migmatite transition of the Aoyama area**

384

385 Mechanism of zircon growth in the Aoyama area

386

387 The modal amount of zircon ($> 20 \mu\text{m}$) is high in schists of the Grt-Crd zone, and is lower in
388 metatexites (Fig. 2). This tendency is not controlled by the difference in the whole-rock Zr
389 concentration, because it is observed for the schists and metatexites showing similar whole-rock Zr
390 concentration (Table 1, Fig. 2). Figure 2 shows that about 60% of the whole-rock Zr is contained in
391 zircon ($> 20 \mu\text{m}$) in the schists, whereas less than 40% of the whole-rock Zr is contained in zircon ($>$
392 $20 \mu\text{m}$) in metatexites. In diatexites, 30-50% of whole-rock Zr can be accounted for by the presence
393 of zircon ($> 20 \mu\text{m}$), which is higher than the metatexites case. From the CSD plot of the metatexite
394 sample AN44 (Fig. 3), abundant occurrence of fine-grained zircon ($< 20 \mu\text{m}$) is confirmed, and from
395 a modal amount calculation of fine-grained zircon, roughly 20-40% of whole-rock Zr resides in
396 zircon ($< 20 \mu\text{m}$), assuming rounded shape of them. This suggests that tiny zircon grains are the

397 important carrier of whole-rock Zr.

398 Angular shape of the core of zircon in metatexites and diatexites (Figs. 5a-b, i-j, 9e-f, k-l, q-r)
399 suggests that these cores did not resorb (Vavra et al. 1999), and the rim grew without experiencing
400 resorption. Since the zircon included in peritectic garnet has tiny inclusion alignment and dark-CL
401 annulus that resemble to melt-inclusion-bearing zircon in diatexites, the rim overgrowth on angular
402 core probably occurred in the presence of melt.

403 The source of Zr for this rim overgrowth is problematic. One possible source of Zr required for
404 the rim overgrowth is the breakdown of Zr-bearing phases other than zircon. Biotite is not an
405 important sink of Zr (Bea et al. 2006), and thus biotite breakdown cannot supply sufficient Zr. The
406 Zr-bearing phases like garnet (Fraser et al. 1997) and ilmenite (Bingen et al. 2001) are the product of
407 the partial melting reaction (2) rather than the reactant, so they cannot provide Zr, either. Minor
408 xenotime (Bea et al. 2006) can be a Zr source for zircon overgrowth, but the microstructural
409 evidence for this is absent so far. Therefore, breakdown of Zr-bearing phases other than zircon is less
410 likely.

411 Accepting that Zr is mostly hosted in zircon (Fraser et al. 1997), and because tiny zircon grains
412 are confirmed to be an important carrier of Zr in samples of this study (Figs. 3, 4), behavior of tiny
413 zircon grains is a key to understand the mechanism of zircon growth. Because the inherited core of
414 zircon in metatexites and diatexites often exceeds 5-10 μm , it is possible that zircon grains less than
415 this size were selectively dissolved through the Ostwald ripening process in the presence of melt at
416 the initial stage of zircon growth (e.g. Vavra et al. 1999). Microstructural observation requests this
417 process if the Zr is not introduced externally, although the observed CSD pattern does not directly
418 support this process. However, the CSD pattern does not deny the Ostwald ripening at the initial
419 stage of zircon growth, since our data does not cover the fine-grained zircon population as 5-10 μm
420 size except for Fig. 3, and the evidence for an early stage process in CSD pattern could be erased by
421 the later processes (e.g. Cashman and Ferry 1988). Judging from the fact that zircon inclusion in
422 peritectic garnet also has an overgrowth accompanying dark-CL annulus and tiny inclusions, this
423 process took place during the near-peak metamorphism.

424 The linear CSD plots generally suggest the continuous nucleation and growth of zircon grains
425 during metamorphism (e.g. Cashman and Ferry 1988; Okudaira 1996). However, as is clear from
426 microstructural observation and LA-ICP-MS dating of zircon, inherited cores are abundant in zircon
427 (Figs. 5, 8, 9). Therefore, theories and interpretation valid for crystals without inherited cores should
428 not be applied directly to this study. A linear CSD trend is even observed for the pelitic schist sample
429 AN24, in which development of zircon overgrowth is not evident (Fig. 8q-v). Therefore, it is highly
430 possible that this linear CSD trend was already acquired at the protolith stage.

431 However, the ca. 35 μm zircon grains with ca. 90 Ma age (Fig. 5m-n), probably representing
432 newly nucleated grains, are common in diatexites. Therefore, fine-grained portion of the CSD plots

433 for diatexites, at least, could potentially represent the mechanism of zircon growth during the Ryoke
434 metamorphism. The CSD plots of diatexite sample Y32A (Fig. 4h) shows curved nature at the finest
435 grain size range ($< 35 \mu\text{m}$). This could represent the later modification of originally linear CSD
436 pattern by the Ostwald ripening process (Cashman and Ferry 1988). Therefore, we consider that
437 growth of zircon grains at the near-peak metamorphic stage occurred through the Ostwald ripening
438 process consuming finer-grained zircon than ca. $35 \mu\text{m}$ in the diatexite sample Y32A.

439

440

Interpretation of the dark-CL annulus and melt inclusions

441

442 Zircon ($> 20 \mu\text{m}$) in the schists is inherited, detrital grain that is evident from the LA-ICP-MS
443 U-Pb zircon dating giving various old ages (Fig. 8). Cretaceous overgrowth on them is very thin or
444 almost absent. However in metatexites, young-aged overgrowth (ca. 90 Ma) is developed in most of
445 the zircon grains as suggested by the presence of zircon rim with similar microstructural
446 characteristics to melt-inclusion-bearing diatexite zircon (Fig. 9), and by the presence of ca. 90 Ma
447 lower intercept for mixed analysis of zircon core and rim (Fig. 10). The ca. 90 Ma rim is commonly
448 separated from the inherited, detrital core by the melt inclusion alignments included in a thin, dark
449 annulus observed under the CL image (Figs. 5, 9). This trend is much clear in diatexites. Since
450 dark-CL annulus is commonly developed on the inherited core of various ages, it is not
451 contemporaneous with the inherited core, but is rather a part of an overgrowth contemporaneous
452 with the ca. 90 Ma rim.

453 This kind of dark-CL overgrowth on the inherited core of the Ivrea Zone is considered to have
454 formed during the amphibolite facies metamorphism (Vavra et al. 1999). In the Aoyama area, garnet
455 porphyroblasts in metatexites and diatexites include zircon ($< 20 \mu\text{m}$) with microstructure very
456 similar to the melt-inclusion-bearing dark-CL annulus (Figs. 5, 9). Since garnet is considered to be a
457 product of near-peak metamorphism, this clearly shows that melt inclusions, dark-CL annulus and
458 part of the brighter-CL overgrowth on the dark-CL annulus (all found in zircon inclusions in garnet)
459 are all formed at the near-peak metamorphism. Cesare et al. (2009) also interprets the zircon with
460 euhedral overgrowths included in garnet from El Hoyazo to have formed early in the melting
461 process.

462 However, this dark-CL annulus is commonly truncated by the bright-CL overgrowth in
463 diatexites (Fig. 5a-b). Therefore, resorption of relatively coarse-grained zircon took place after the
464 near-peak growth of zircon. Such a resorption can occur when the amount of melt increased and the
465 fine-grained zircon was totally consumed. Resorption of zircon continues as far as the amount of
466 melt increases, but it starts to crystallize when the melt starts to cool and crystallize and the
467 solubility of Zr in the melt decreases. Therefore, timing of the bright-CL overgrowth development
468 that truncates dark-CL annulus is the retrograde, melt crystallization stage.

469 To summarize, zircon rim overgrowth (the dark-CL annulus and an outer part than it) is partly
470 near-peak metamorphic in origin, and partly retrograde. Therefore, the U-Pb ages for zircon rims and
471 newly nucleated grains obtained in this study represent the mixed age of near-peak and retrograde
472 zircons, although the contribution of the near-peak zircon is small in some cases. For example, the
473 analysis spot giving 90 ± 8 Ma in Fig. 5a-b is completely retrograde in origin because the rim
474 analyzed truncates both the dark-CL annulus and part of the bright-CL overgrowth on it. The timing
475 of this zircon rim crystallization is dated to be 90.3 ± 2.2 Ma (Table 3, Fig. 7b). The low Th/U ratio
476 of these young zircon rims (Fig. 5, Table 3) would be due to the coexistence with monazite during its
477 growth (Kawakami and Suzuki 2011; Cesare et al. 2003), as shown by the presence of monazite and
478 zircon with rim overgrowth included in garnet.

479 A fluid activity during the contact metamorphic event at 83.5 ± 2.4 Ma detected by the CHIME
480 monazite dating is considered responsible for the rejuvenation of the monazite age (Kawakami and
481 Suzuki 2011). Absence of further young overgrowth or rejuvenated part in zircon suggests that
482 zircon was almost immune from the contact metamorphic event at 83.5 ± 2.4 Ma (Kawakami and
483 Suzuki 2011). Overall discussion above suggests that presence of the melt is playing an important
484 role in zircon formation during the high-temperature metamorphism (e.g. Vavra et al. 1999; Rubatto
485 et al. 2001) in the Ryoke metamorphic belt at the Aoyama area.

486

487 Duration of the high-temperature, low-pressure type Ryoke metamorphism

488

489 Monazite in the Ryoke metamorphic belt has been considered to record the timing of prograde
490 growth when the rock first attained 525 °C (e.g. Suzuki and Adachi 1998). We follow their
491 interpretation that the CHIME monazite age of 96.5 ± 1.9 Ma in the Aoyama area (Kawakami and
492 Suzuki 2011) represents the timing of monazite growth at around 525 °C. On the other hand, zircon
493 rims and newly nucleated grains give the mixed age of the near-peak metamorphism to the
494 retrograde, melt crystallization stage (90.3 ± 2.2 Ma; Fig. 7b). The retrograde crystallization of
495 zircon can be the same as or younger than this age. Therefore, using the difference of growth timing
496 of monazite and zircon in the Aoyama area, duration of metamorphism higher than the amphibolite
497 facies grade could be estimated (Fig. 11). These give the duration of high-temperature, low-pressure
498 type Ryoke metamorphism of at least ca. 6 Myr in the case of the Aoyama area. This is a little longer
499 than the estimate of Suzuki et al. (1994) who considered the duration of the Ryoke metamorphism
500 above ca. 500 °C to be about 5 Myr.

501

502

Acknowledgements

503

504 We would like to thank Takamoto Okudaira and Bernardo Cesare for constructive reviews and

505 Timothy L. Grove for editorial efforts. Thanks are also due to Fumiko Higashino and Takao Hirajima
506 for LA-ICP-MS analysis, and Akira Tsuchiyama and Toru Matsumoto for FE-SEM analysis. This
507 study was supported by the Grant-in-Aid for Young Scientists (B) (23740391, Tetsuo Kawakami)
508 and Grant-in-Aid for Scientific Research (A) (22244067, Takao Hirajima) from JSPS and MEXT.

509

510

References

511

512 Bea, F, Montero, P, Ortega, M (2006) A LA-ICP-MS evaluation of Zr reservoirs in common crustal
513 rocks: Implications for Zr and Hf geochemistry, and zircon-forming processes. *The Canadian*
514 *Mineralogist* 44: 693-714

515 Bingen, B, Austrheim H, Whitehouse M (2001) Ilmenite as a source for zirconium during
516 high-grade metamorphism? Textural evidence from the Caledonides of Western Norway and
517 implications for zircon geochronology. *Journal of Petrology* 42: 355-375

518 Bowman JR, Moser DE, Valley JW, Wooden JL, Kita NT, Mazdab FK (2011) Zircon U-Pb isotope,
519 $\delta^{18}\text{O}$ and trace element response to 80 m.y. of high temperature metamorphism in the lower
520 crust; sluggish diffusion and new records of Archean craton formation. *American Journal of*
521 *Science* 311: 719-772

522 Brown M (1998) Unpairing metamorphic belts: P-T paths and a tectonic model for the Ryoke Belt,
523 southwest Japan. *Journal of Metamorphic Geology* 16: 3-22

524 Cashman KV, Ferry JM (1988) Crystal size distribution (CSD) in rocks and kinetics and dynamics of
525 crystallization. *Contributions to Mineralogy and Petrology* 99: 401-415

526 Cesare B, Acosta-Vigil A, Ferrero S, Bartoli O (2011) Melt inclusions in migmatites and granulites.
527 *Journal of the Virtual Explorer* 38: paper 2, doi: 10.3809/jvirtex.2011.00268

528 Cesare B, Gomez-Pugnaire MT, Rubatto D (2003) Residence time of S-type anatectic magmas
529 beneath the Neogene Volcanic Province of SE Spain: a zircon and monazite SHRIMP study.
530 *Contributions to Mineralogy and Petrology*: 146 28-43

531 Cesare B, Rubatto D, Go´mez-Pugnaire MT (2009) Do extrusion ages reflect magma generation
532 processes at depth? An example from the Neogene Volcanic Province of SE Spain.
533 *Contributions to Mineralogy and Petrology* 157: 267-279

534 Corfu F, Hanchar JM, Hoskin PWO, Kinny P (2003) Atlas of zircon textures. *Reviews in Mineralogy*
535 *and Geochemistry* 53: 469-500

536 Eggins SM, Kinsley LPJ, Shelley JMG (1998) Deposition and element fractionation processes
537 during atmospheric pressure laser sampling for analysis by ICP-MS. *Applied Surface Science*
538 129: 278-286

539 Fraser G, Ellis D, Eggins S (1997) Zirconium abundance in granulite-facies minerals, with
540 implications for zircon geochronology in high-grade rocks. *Geology* 25: 607-610

541 Geisler T, Schaltegger U, Tomaschek F (2007) Re-equilibration of zircon in aqueous fluids and melts.
542 Elements 3: 43-50

543 Goto A, Tatsumi Y (1996) Quantitative analysis of rock samples by an X-ray fluorescence
544 spectrometer (II). Rigaku Journal 13: 20- 38

545 Gunther D, Heinrich CA (1999) Enhanced sensitivity in laser ablation-ICP mass spectrometry using
546 He-Ar mixtures as aerosol carrier. Journal of Analytical Atomic Spectrometry 14: 1363-1368

547 Harley SL, Kelly NM, Moller A (2007) Zircon behaviour and thermal histories of mountain chains.
548 Elements 3: 25-40

549 Hayama Y, Yamada T, Ito M, Kutsukake T, Masaoka K, Miyakawa K, Mochizuki Y, Nakai Y,
550 Tainosho Y, Yoshida M, Kawarabayashi I, Tsumura Y (1982) Geology of the Ryoke Belt in the
551 eastern Kinki District, Japan -The phase-divisions and the mutual relations of the granitic rocks-.
552 Journal of the Geological Society of Japan 88: 451-466 (in Japanese with English abstract)

553 Higashino F, Kawakami T, Satish-Kumar M, Ishikawa M, Maki K, Tsuchiya N, Grantham G, Hirata
554 T (2012) Chlorine-rich fluid or melt activity during granulite facies metamorphism in the Late
555 Proterozoic to Cambrian continental collision zone – an example from the Sør Rondane
556 Mountains, East Antarctica. Precambrian Research *in press*

557 Hirata T, Iizuka T, Orihashi Y (2005) Reduction of mercury background on ICP-mass spectrometry
558 for in situ U-Pb age determinations of zircon samples. Journal of Analytical Atomic
559 Spectrometry 20: 696-701

560 Iizuka T, Hirata T (2004) Simultaneous determinations of U-Pb age and REE abundances for zircons
561 using ArF excimer laser ablation-ICPMS. Geochemical Journal 38: 229-241

562 Ikeda T (1998a) Progressive sequence of reactions of the Ryoke metamorphism in the Yanai district,
563 southwest Japan: the formation of cordierite. Journal of Metamorphic Geology 16: 39-52

564 Ikeda T (1998b) Phase equilibria and the pressure-temperature path of the highest-grade Ryoke
565 metamorphic rocks in the Yanai district, SW Japan. Contributions to Mineralogy and Petrology
566 132: 321-335

567 Ikeda T (2002) Regional occurrence of orthopyroxene-bearing basic rocks in the Yanai district, SW
568 Japan: evidence for granulite-facies Ryoke metamorphism. Island Arc 11: 185-192

569 Jackson SE, Pearson NJ, Griffin WL, Belousova EA (2004) The application of laser
570 ablation-inductively coupled plasma-mass spectrometry to in situ U-Pb zircon geochronology.
571 Chemical Geology 211: 47-69

572 Jaffey AH, Flynn KF, Glendenin LE, Bentley WC, Essling AM (1971) Precision measurement of
573 half-lives and specific activities of ^{235}U and ^{238}U . Physical Review C 4: 1889-1906

574 Kawakami T (2001a) Tourmaline breakdown in the migmatite zone of the Ryoke metamorphic belt,
575 SW Japan. Journal of Metamorphic Geology 19: 61-75

576 Kawakami T (2001b) Boron depletion controlled by the breakdown of tourmaline in the migmatite

577 zone of the Aoyama area, Ryoke metamorphic belt, SW Japan. *Canadian Mineralogist* 39:
578 1529-1546

579 Kawakami T (2002) Magmatic andalusite from the migmatite zone of the Aoyama area, Ryoke
580 metamorphic belt, SW Japan, and its importance in constructing the P-T path. *Journal of*
581 *Mineralogical and Petrological Sciences* 97: 241-253

582 Kawakami T (2004) Tourmaline and boron as indicators of the presence, segregation and extraction
583 of melt in pelitic migmatites: examples from the Ryoke metamorphic belt, SW Japan.
584 *Transactions of the Royal Society of Edinburgh: Earth Sciences* 95: 111-124

585 Kawakami T, Ikeda T (2003) Depletion of whole-rock boron controlled by the breakdown of
586 tourmaline and retrograde formation of borosilicates in the Yanai area, Ryoke metamorphic belt,
587 SW Japan. *Contributions to Mineralogy and Petrology* 145: 131-150

588 Kawakami T, Kobayashi T (2006) Trace element composition and the degree of partial melting of
589 pelitic migmatites from the Aoyama area, Ryoke metamorphic belt, SW Japan: Implications for
590 the source region of tourmaline leucogranites. *Gondwana Research* 9: 176-188

591 Kawakami T, Nishioka Y (2012) Metamorphic rocks and granitoids in the Aoyama area, Ryoke belt,
592 SW Japan. *Journal of the Geological Society of Japan* 118 Supplement: 79-89 (in Japanese)

593 Kawakami T, Suzuki K (2011) CHIME monazite dating as a tool to detect polymetamorphism in
594 high-temperature metamorphic terrane – an example from the Aoyama area, Ryoke metamorphic
595 belt, SW Japan. *Island Arc* 20: 439-453

596 Kretz R (1983) Symbols for rock-forming minerals. *American Mineralogist* 68: 277-279

597 Ludwig KR (2008) User's manual for Isoplot 3.6. A geological toolkit for Microsoft Excel. Berkeley
598 Geochronology Center Special Publication No.4, revision of April 8, 2008. 77p.

599 Mahar EM, Baker JM, Powell R, Holland TJB, Howell N (1997) The effect of Mn on mineral
600 stability in metapelites. *Journal of Metamorphic Geology* 15: 223-238

601 Miyashiro A (1965) *Metamorphic Rocks and Metamorphic Belts*. Iwanami Shoten Publishers, Tokyo.
602 458p. (in Japanese)

603 Morishita R (1992) Crystal size distribution of Togawa andesite lava. *Bulletin of Volcanological*
604 *Society of Japan* 37: 285-293 (in Japanese with English abstract)

605 Nakajima T (1994) The Ryoke plutonometamorphic belt: Crustal section of the Cretaceous Eurasian
606 continental margin. *Lithos* 33: 51-66

607 Okudaira T (1996) Temperature-time path for the low-pressure Ryoke metamorphism, Japan, based
608 on chemical zoning in garnet. *Journal of Metamorphic Geology* 14: 427-440

609 Okudaira T, Hara I, Sakurai Y, Hayasaka Y (1993) Tectono-metamorphic processes of the Ryoke belt
610 in the Iwakuni-Yanai district, southwest Japan. *Memoirs of the Geological Society of Japan* 42:
611 91-120

612 Ozaki M, Sangawa A, Miyazaki K, Nishioka Y, Miyachi Y, Takeuchi K, Tagutschi Y (2000) *Geology*

- 613 of the Nara District. With Geological Sheet Map at 1 : 50,000, Geological Survey of Japan, 162p.
614 (in Japanese with English abstract 5p.)
- 615 Rubatto D, Hermann J (2007) Zircon behavior in deeply subducted rocks. *Elements* 3: 31-35
- 616 Rubatto D, Williams IS, Buick IS (2001) Zircon and monazite response to prograde metamorphism
617 in the Reynolds Range, central Australia. *Contributions to Mineralogy and Petrology* 140:
618 458-468
- 619 Schaltegger U, Fanning CM, Gunter D, Maurin JC, Schlmann K, Gebauer D (1999) Growth,
620 annealing and recrystallization of zircon and preservation of monazite in high-grade
621 metamorphism: conventional and in-situ U-Pb isotope, cathodoluminescence and microchemical
622 evidence. *Contributions to Mineralogy and Petrology* 134: 186-201
- 623 Schiøtte L, Compston W, Bridgwater D (1989) Ion probe U-Th-Pb zircon dating of
624 polymetamorphic orthogneisses from northern Labrador, Canada. *Canadian Journal of Earth
625 Sciences* 26: 1533-1556
- 626 Stacey JS, Kramers JD (1975) Approximation of terrestrial lead isotope evolution by a two-stage
627 model. *Earth and Planetary Science Letters* 26: 207-221
- 628 Suzuki K, Adachi M (1998) Denudation history of the high T/P Ryoke metamorphic belt, southwest
629 Japan: constraints from CHIME monazite ages of gneisses and granitoids. *Journal of
630 Metamorphic Geology* 16: 23- 37
- 631 Suzuki K, Adachi M, Kajizuka I (1994) Electron microprobe observations of Pb diffusion in
632 metamorphosed detrital monazites. *Earth and Planetary Science Letters* 128: 391-405
- 633 Tainosho Y, Kagami H, Yuhara M, Nakano S, Sawada K, Morioka K (1999) High initial Sr isotopic
634 ratios of Cretaceous to Early Paleogene granitic rocks in Kinki district, Southwest Japan. *The
635 memoirs of the Geological Society of Japan* 53: 309-321
- 636 Takahashi Y, Nishioka Y (1994) Mode of plagioclase twinnings in Ryoke metamorphic rocks in the
637 western area of Tsu City, Mie Prefecture. *Journal of the Japanese Association of Mineralogist,
638 Petrologists and Economic Geologists* 89: 261-268 (in Japanese with English abstract)
- 639 Thomas JB, Bodnar RJ, Shimizu N, Chesner CA (2003) Melt inclusions in zircon. *Reviews in
640 Mineralogy and Geochemistry* 53: 63-87
- 641 Tunheng A, Hirata T (2004) Development of signal smoothing device for precise elemental analysis
642 using laser ablation-ICP-mass spectrometry. *Journal of Analytical Atomic Spectrometry* 19:
643 932-934
- 644 Vavra G, Gebauer D, Schmid R, Compston W (1996) Multiple zircon growth and recrystallization
645 during polyphase Late Carboniferous to Triassic metamorphism in granulites of the Ivrea Zone
646 (Southern Alps): an ion microprobe (SHRIMP) study. *Contributions to Mineralogy and
647 Petrology* 122: 337-358
- 648 Vavra G, Schmid R, Gebauer D (1999) Internal morphology, habit and U-Th-Pb microanalysis of

649 amphibolite-to-granulite facies zircons: geochronology of the Ivrea Zone (Southern Alps).
650 Contributions to Mineralogy and Petrology 134: 380-404

651 Wakita K (1987) The occurrence of Latest Jurassic - Earliest Cretaceous radiolarians at the
652 Hida-Kanayama area in the Mino terrane, central Japan. The Journal of Geological Society of
653 Japan 93: 441-443

654 Wei CJ, Powell R, Clarke GL (2004) Calculated phase equilibria for low- and medium-pressure
655 metapelites in the KFMASH and KMnFMASH systems. Journal of Metamorphic Geology 22:
656 495-508

657 Wiedenbeck M, Alle P, Corfu F, Griffin WL, Meier M, Oberli F, Von Quadt A, Roddick JC, Spiegel
658 W (1995) Three natural zircon standards for U-Th-Pb, Lu-Hf, trace element and REE analyses.
659 Geostandards Newsletter 19: 1-23

660 Wiedenbeck M, Hanchar JM, Peck WH, Sylvester P, Valley J, Whitehouse M, Kronz A, Morishita Y,
661 Nasdala L, Fiebig J, Franchi I, Girard J-P, Greenwood RC, Hinton R, Kita N, Mason PRD,
662 Norman M, Ogasawara M, Piccoli PM, Rhede D, Satoh H, Schulz-Dobrick D, Skår Ø, Spicuzza
663 MJ, Terada K, Tindle A, Togashi S, Vennemann T, Xie Q, Zheng Y-F (2004) Further
664 characterisation of the 91500 zircon crystal. Geostandards and Geoanalytical Research 28: 9-39.

665 Yoshida F, Takahashi Y, Nishioka Y (1995) Geology of the Tsu-Seibu district. With geological sheet
666 map at 1:50,000. Geological Survey of Japan. (in Japanese with English abstract)

667 Yoshizawa H, Nakajima W, Ishizaka K (1966) The Ryoke metamorphic zone of the Kinki district,
668 Southwest Japan: Accomplishment of a regional geological map. Memoirs of the College of
669 Science, University of Kyoto, Series B 32: 437-453

670
671

672 **Figure captions**

673 Fig. 1 (a) Simplified geological map of the Ryoke metamorphic belt. The low-temperature,
674 high-pressure type Sanbagawa belt is located to the south of the Ryoke metamorphic belt and
675 these two belts are separated by the Median Tectonic Line (MTL). (b) Geological map of the
676 Aoyama area (after Yoshida et al. 1995; Ozaki et al. 2000) showing the sample localities. The
677 Grt-Crd and tourmaline-out isograds (Kawakami 2001a) are subparallel to the schist/migmatite
678 boundary and to the penetrative schistosity and migmatitic banding observed in this area.
679 Sample names shown next to locality points correspond to those given in Table 1.

680

681 Fig. 2. A diagram showing the whole-rock Zr concentration versus modal amount of zircon (> 20
682 μm). Density of the rock and zircon were assumed to be 2.7 g/cm^3 and 4.6 g/cm^3 , respectively.
683 Each diamond and square pair connected by a solid line represent a dataset from a single sample,
684 based on the different assumption made in calculating the modal amount of zircon in a single

685 thin section as follows: (i) assuming ellipsoidal shape of zircon, plotted as low-modal amount
686 points, and (ii) assuming rectangular shape of zircon, plotted as high-modal amount points.
687 Broken lines and numbers (%) shown in the figure represents the percentage of whole-rock Zr
688 content hosted by the zircon (> 20 μm).

689

690 Fig. 3 A plot showing the result of grain size distribution of zircon in a metatexite sample AN44,
691 determined by the X-ray elemental mapping of the whole thin section (open diamonds).
692 Numerical expression given in the figure is that for the least squares fit of the solid triangle data
693 (solid line). A broken line represents the least squares fit for the gray square points. See text for
694 further explanation.

695

696 Fig. 4. A summary of the CSD plots for 2 schist samples (Fig. 4a, b), 4 metatexite samples (Fig. 4c-f),
697 and 4 diatexite samples (Fig. 4g-k). All the zircon grain size (major axis) data were measured by
698 BSE image observation utilizing WDS. Sample numbers are given in the top right of each figure
699 (AN32 etc.). See Fig. 1b for the sample locality and Table 1 for sample descriptions. (j) is an
700 enlargement of the fine-grained portion of (i). See text for details.

701

702 Fig. 5. The BSE and CL images of zircon in diatexites from the Grt-Crd zone of the Aoyama area.
703 Red circles represent the size of pits created by LA-ICP-MS U-Pb dating and numbers given are
704 the $^{206}\text{Pb}/^{238}\text{U}$ age \pm 2SD error [better than 95-105% concordance except for the points at young
705 rim of (b) 93%, (f) 93%, and (l) 94%, where concordance = $(^{206}\text{Pb}/^{238}\text{U} \text{ age}) * 100 / (^{207}\text{Pb}/^{235}\text{U}$
706 age)] and Th/U ratio. These relatively low concordance data points are shown so that correlation
707 with zircon microstructure is clear. '*' represents that the point gave discordant data. Scale bars
708 are 10 μm. Red arrows indicate the melt (presently glass) and mineral (biotite, quartz,
709 plagioclase and K-feldspar) inclusions included along the thin, bright annulus under BSE image.
710 This annulus is recognized as dark annulus in CL image. Red dotted line represents the core/rim
711 boundary where dark-CL annulus is truncated by the brighter-CL overgrowth. (a), (c), (e), (g),
712 (i) and (k); CL image of zircon grains from a diatexite (G6-28, G6-31, G6-4, G6-34, G6-38, and
713 G6-17, respectively). (a), (c), (e) and (i) are in the matrix, and (g) and (k) are included in biotite.
714 (b), (d), (f), (h), (j) and (l); BSE images of (a), (c), (e), (g), (i) and (k), respectively. (m) CL
715 image of a newly nucleated zircon grain at 86.7 ± 9.2 Ma present in the matrix of diatexite
716 (Y32-38). Note the similar CL-brightness as the outermost part of the rim overgrowth shown in
717 (a), (c), (e), (g), (i) and (k). (n) BSE image of (m). (o), (q), (s), (u) and (w) CL images of zircon
718 grains from a garnet-bearing diatexite (G11-19, G11-13, G11-16, G11-21 and G11-18,
719 respectively). (q) occurs as an inclusion in garnet, and others are found in the matrix. (w) has
720 tiny inclusion alignment along a dark-CL annulus under transmitted light microscope, but not

721 exposed on the surface. (p), (r), (t), (v) and (x); BSE images of (o), (q), (s), (u) and (w).

722

723 Fig. 6. Bright and dark field images of TEM sample as a whole (sample G6), enlargement of
724 inclusions in it (inclusions 1-5) and electron diffraction patterns of the inclusions. Width of the
725 sample is 9.2 μm . Host mineral of the inclusions is zircon. Diffuse halo pattern clearly shows
726 that inclusions are the glass (inclusions 1, 3 and 5), or the mixture of the glass and crystal
727 (inclusions 2 and 4). Most of the spotted electron diffraction patterns are from host zircon except
728 for inclusions 2 and 4. Red arrows shown in the photo of inclusion 2 are 'nano-porosities' after
729 Cesare et al. (2011). The EDS analysis under TEM shows that inclusion 3 is a glass containing K,
730 Al and Si, and inclusion 1 is a Si-rich glass.

731

732 Fig. 7. (a) Concordia diagram for the LA-ICP-MS U-Pb dating of zircon from the diatexite-dominant
733 part of the Grt-Crd zone. Concordia diagrams in this study are constructed using Isoplot 3.6
734 (Ludwig 2008). Since the thickness of rim and the size of the newly-nucleated zircon sometimes
735 reach more than 20 μm in the diatexite-dominant part of the Grt-Crd zone, LA-ICP-MS dating
736 of the rim can be done without any mixing of the core. However, some of the analyses are the
737 mixed analysis of the core and the rim, resulting in the discordia-like mixing line. Inset is an
738 enlargement of the young-aged part. (b) Concordia diagram for selected analyses of zircon rim
739 and newly-nucleated zircon grain. The result of concordia age calculation is also shown.

740

741 Fig. 8. The BSE and CL images of zircon in a psammitic schist AN16 and a pelitic schist AN24 from
742 the Grt-Crd zone. Red circles represent the size of pits created by LA-ICP-MS U-Pb dating and
743 numbers given are the $^{206}\text{Pb}/^{238}\text{U}$ age \pm 2SD error. (a), (c), (e), (g), (i), (k), (m), (o), (q), (s) and
744 (u); BSE images of zircon. (a) AN16-re13 in matrix, (c) AN16-11 in matrix, (e) AN16-13 in
745 matrix, (g) AN16-07 in matrix, (i) AN16-24 in matrix, (k) AN16-re35 in matrix, (m) AN16-22 in
746 matrix, (o) AN16-29 in matrix, (q) AN24-31 in matrix, (s) AN24-re02 in quartz, and (u)
747 AN24-re15 in plagioclase, respectively. (b), (d), (f), (h), (j), (l), (n), (p), (r), (t) and (v); CL
748 images of (a), (c), (e), (g), (i), (k), (m), (o), (q), (s) and (u).

749

750 Fig. 9. The BSE and CL images of zircon in metatexites from the Grt-Crd zone. Red arrows indicate
751 the melt and mineral inclusions included along the thin, bright annulus under BSE image
752 (identical with the dark-CL annulus). Red circles represent the size of pits created by
753 LA-ICP-MS U-Pb dating and numbers given are the $^{206}\text{Pb}/^{238}\text{U}$ age \pm 2SD error. (a), (c), (e), (g),
754 (i), (k), (m), (o), (q) and (s); CL images of zircon from metatexite samples AN07a, AN27 and
755 AN52. (a) AN07a-1 in garnet, (c) AN07a-3 in retrograde muscovite, (e) AN07-17 in matrix, (g)
756 AN52-25 in matrix, (i) AN07a-2 in garnet, (k) AN07a-12 in matrix, (m) AN07a-07 in biotite, (o)

757 AN52-06 in matrix, (q) AN07-21 in matrix, and (s) AN27-06 in matrix, respectively. (b), (d), (f),
758 (h), (j), (l), (n), (p), (r) and (t); BSE images of (a), (c), (e), (g), (i), (k), (m), (o), (q) and (s).

759

760 Fig. 10. Concordia diagram for the LA-ICP-MS U-Pb dating of zircon from the schist-dominant and
761 metatexite-dominant parts of the Grt-Crd zone. Since the development of the zircon rim is not
762 sufficient enough for LA-ICP-MS dating with 20 μm spot size, mixed analysis was intentionally
763 performed on rims, resulting in the discordia (mixing line) on the diagram. Inset is an
764 enlargement of the young-aged part.

765

766 Fig. 11. A P - T - t path for the low-temperature part of the Grt-Crd zone (schist-migmatite boundary)
767 of the Aoyama area. Modified after Kawakami (2002). Pseudosection shown in the suprasolidus
768 P - T region is from Wei et al. (2004) constructed for KMnFMASH + quartz system using typical
769 pelite composition ($M_{\text{Mn}} = \text{Mn}/(\text{Mn}+\text{Fe}+\text{Mg}) = 0.007$) of Mahar et al. (1997). Their calculation
770 shows that increase of M_{Mn} widens the stability field of garnet + cordierite assemblage very
771 much. With $M_{\text{Mn}} = 0.03$, garnet + cordierite is stable in subsolidus field even at 2 kbar, 650 $^{\circ}\text{C}$
772 (not shown). This is consistent with the whole-rock Mn content of pelitic metamorphic rocks in
773 the Aoyama area (Kawakami 2001b; Kawakami and Kobayashi 2006) and with the field
774 observation that garnet + cordierite assemblage is found not only in migmatite-dominant area
775 but also in the schist-dominant area. Therefore, effect of Mn is responsible for the
776 low-temperature estimates obtained for the Grt-Crd zone samples. Timing of the monazite
777 growth is considered to be the prograde stage (first attainment of 525 $^{\circ}\text{C}$, pressure not
778 constrained; Suzuki and Adachi 1998), and the zircon rim growth to be near-peak metamorphic
779 condition to the retrograde, melt crystallization stage. Zircon rim growth stage is shown by a
780 thick gray arrow.

781

782 Table 1. Summary of the description of samples and the result of whole-rock trace element analyses.

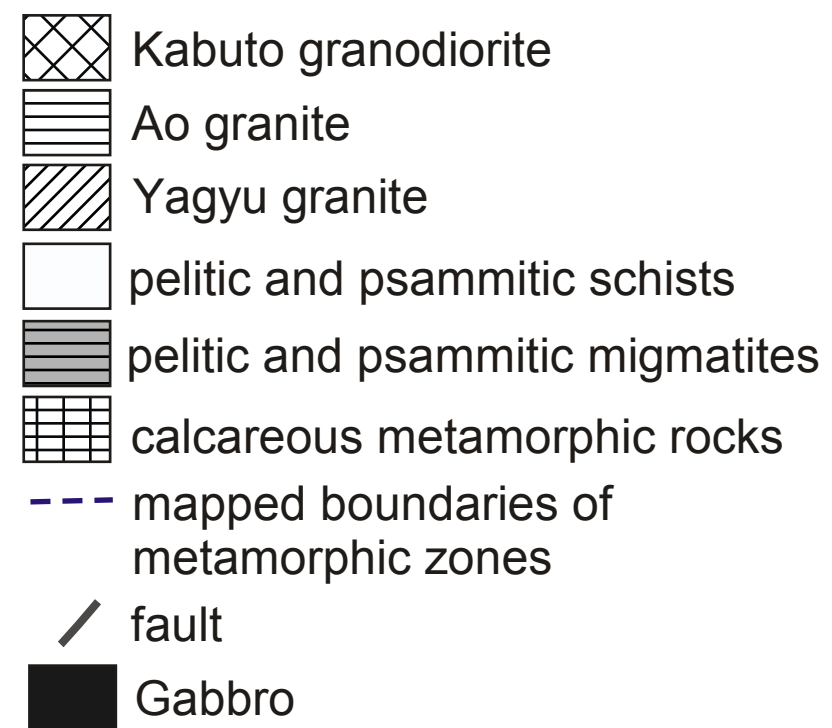
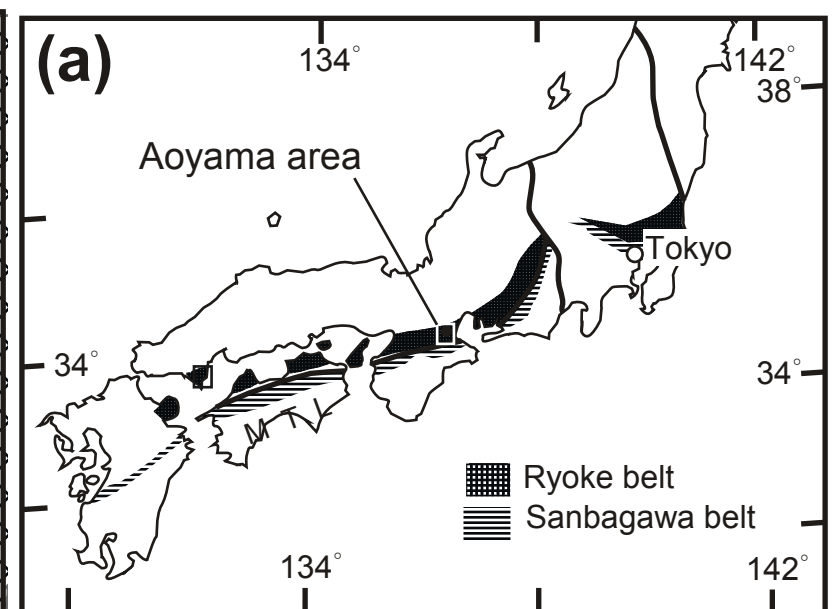
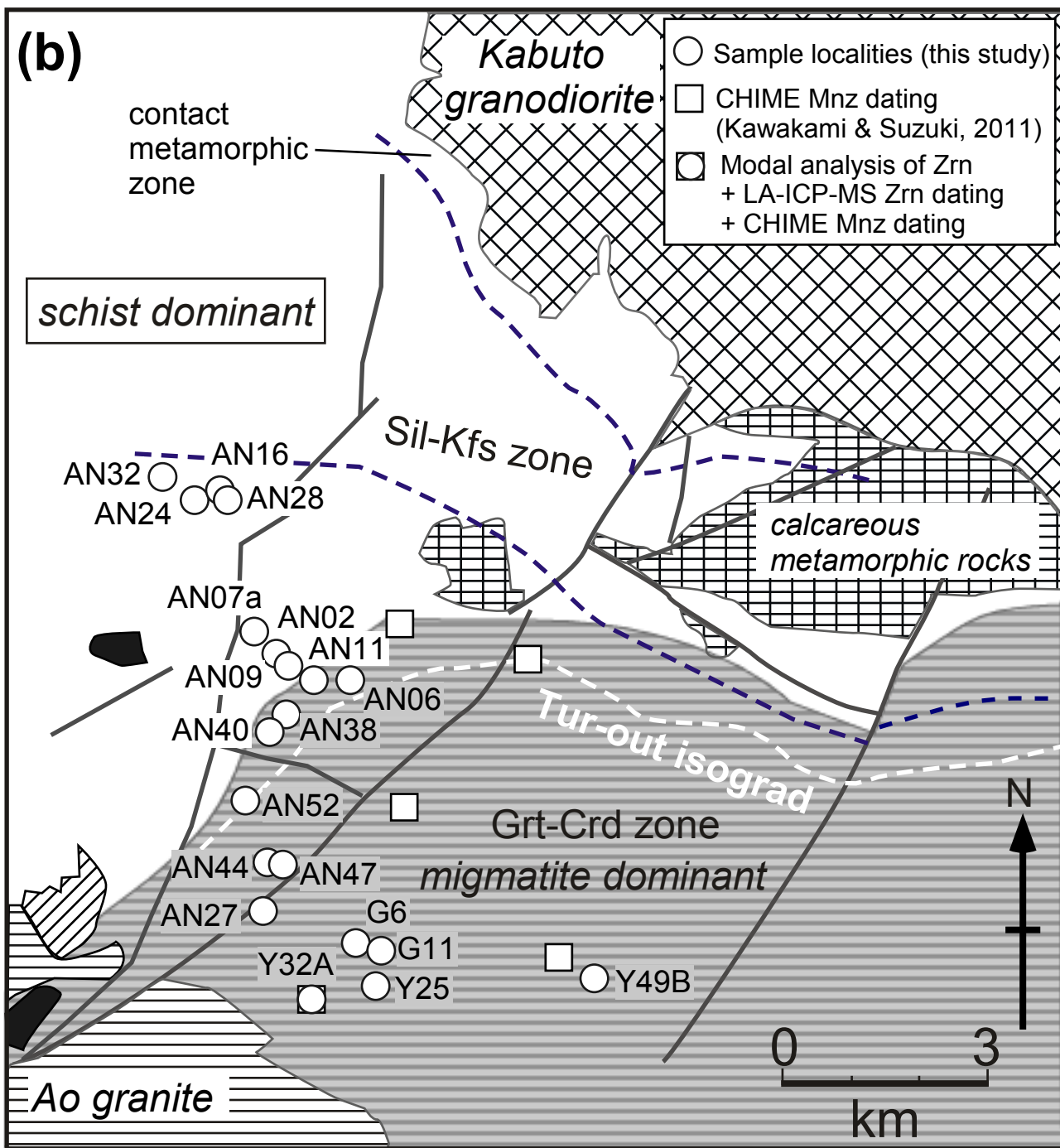
783 Trace element data were obtained for thin-section sized chips by XRF. Crd(?) in the mineral
784 assemblage of sample AN24 represents that alteration that looks like a pseudomorph after Crd is
785 present.

786

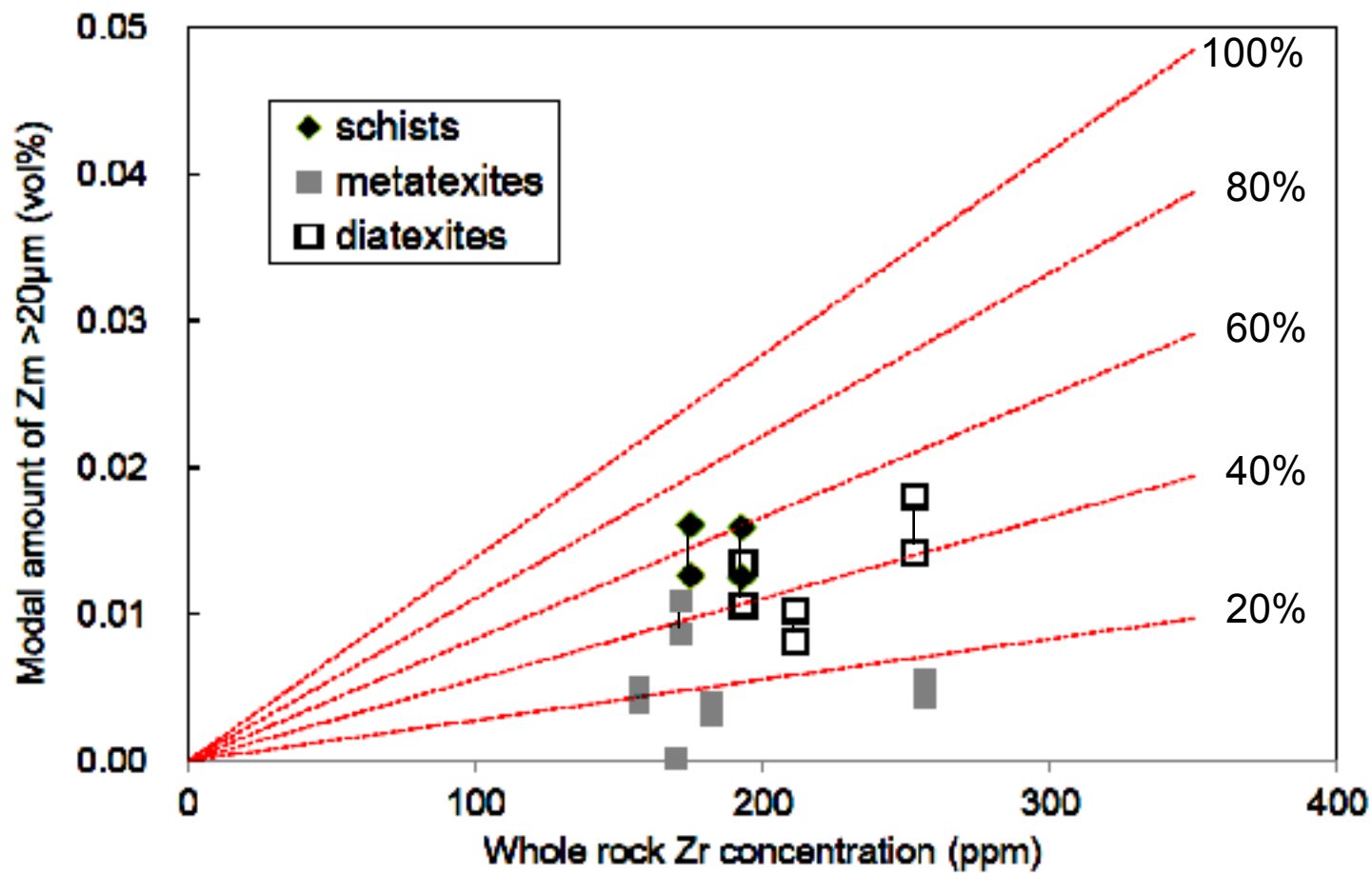
787 Table 2. Instrumental settings of the LA-ICP-MS U-Pb zircon dating at Department of Geology and
788 Mineralogy, Kyoto University.

789

790 Table 3. Representative results of the LA-ICP-MS U-Pb zircon dating that were used for the
791 calculation of 90.3 ± 2.2 Ma concordia age. Most of the ^{204}Pb listed in the table are actually
792 ^{204}Hg as calculated from ^{202}Hg counts. No common Pb correction was applied.



Kawakami et al. Fig. 1



Kawakami et al. Fig. 2

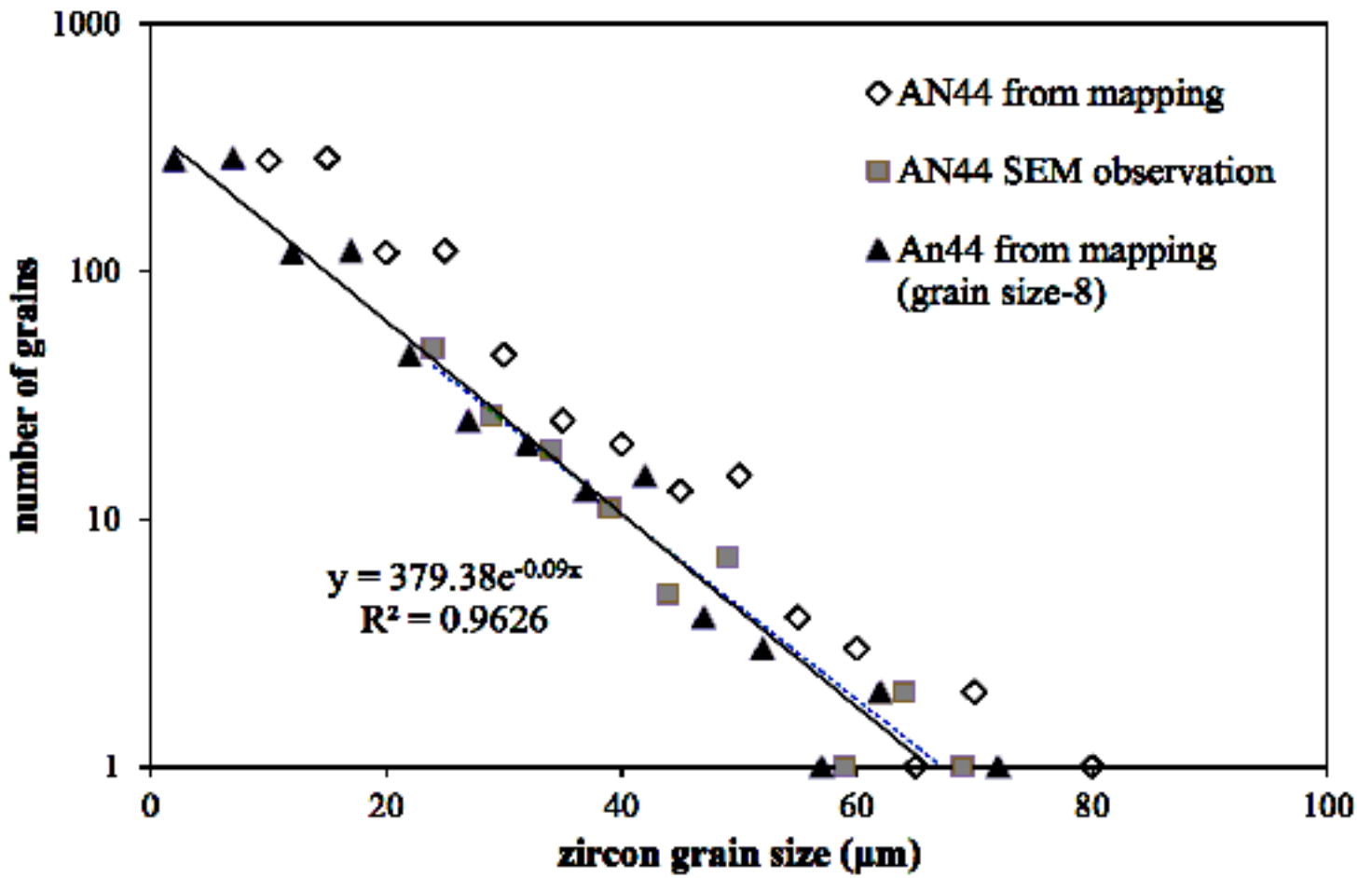


Figure 3 Kawakami et al.

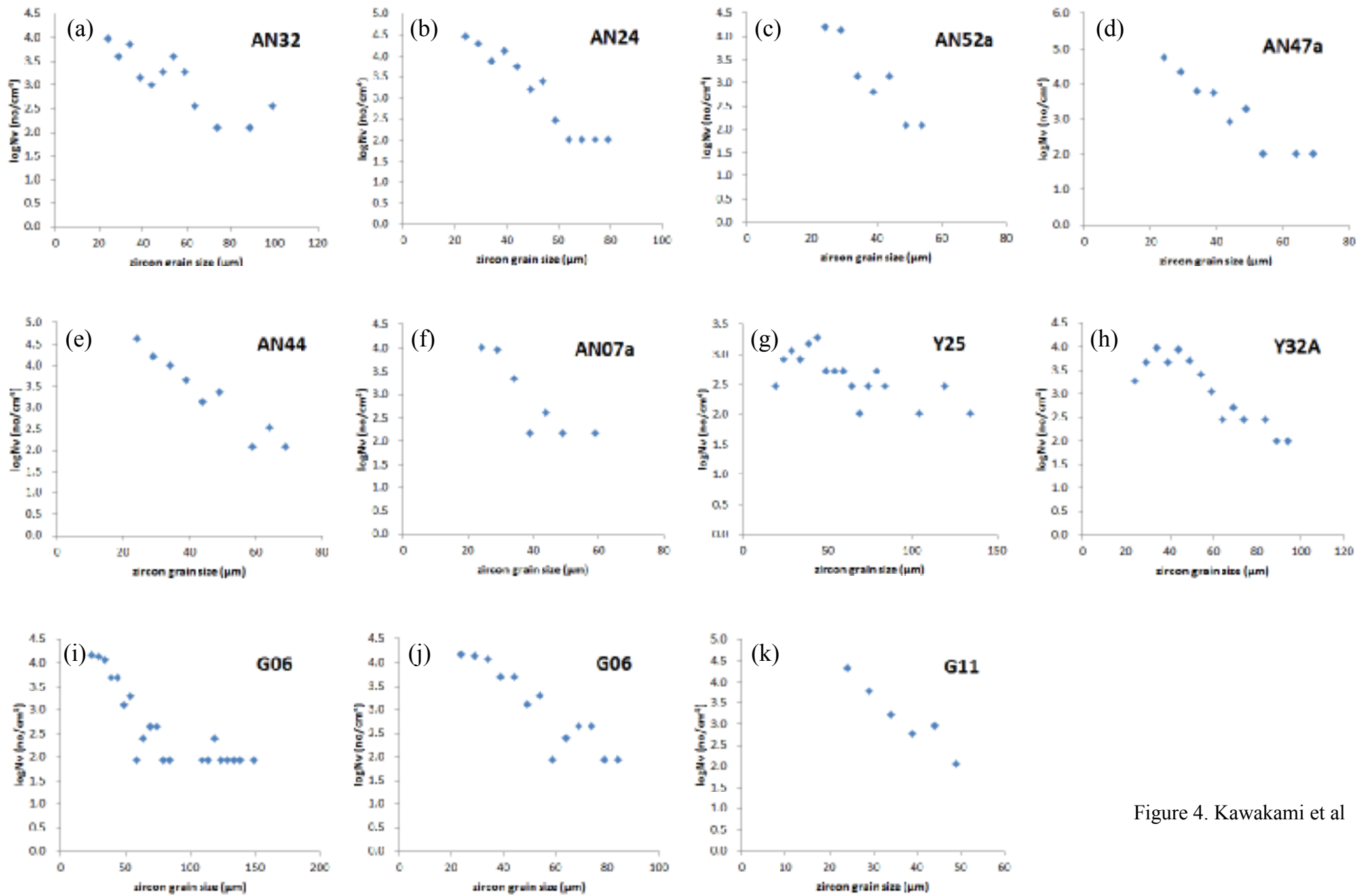
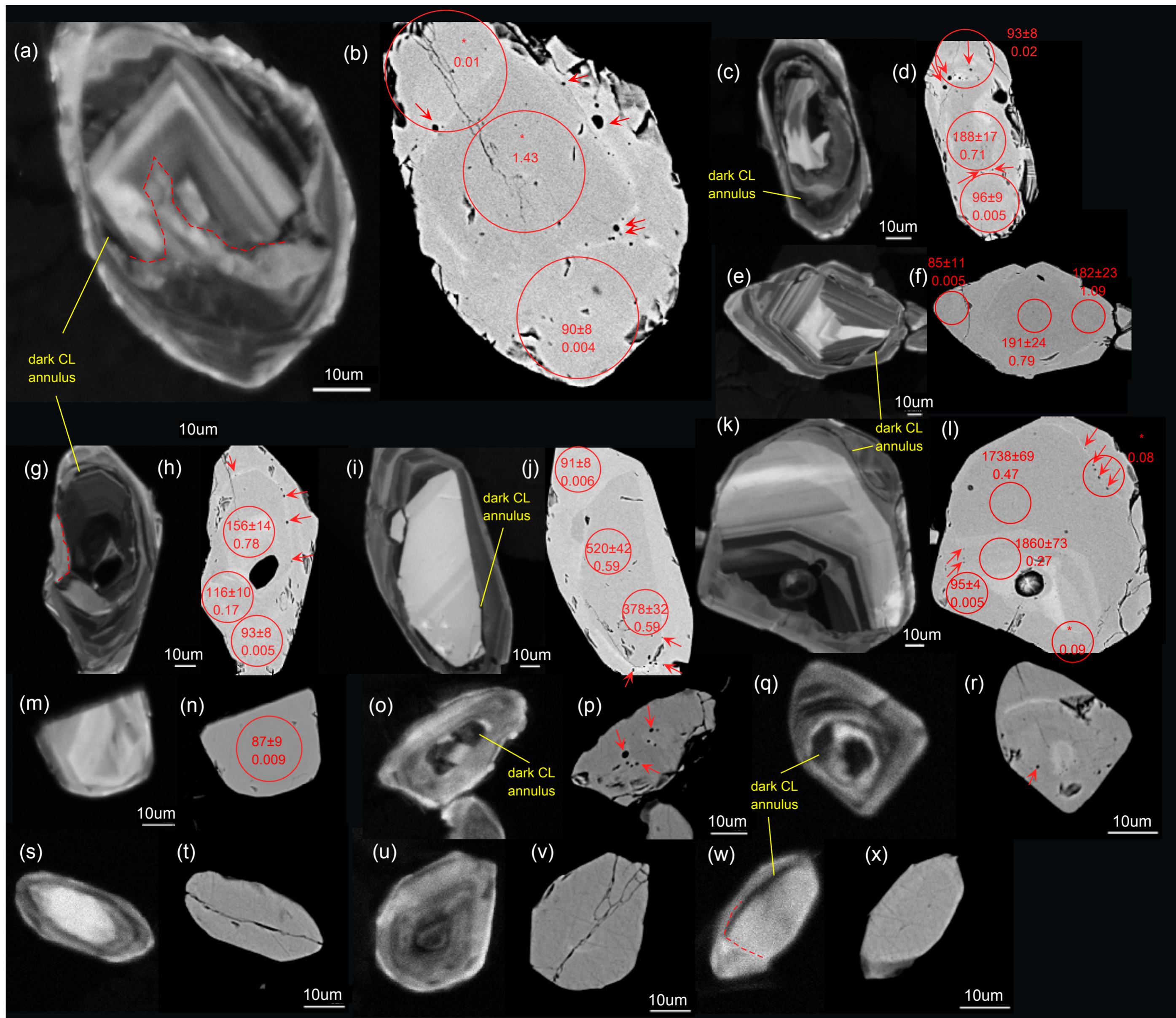
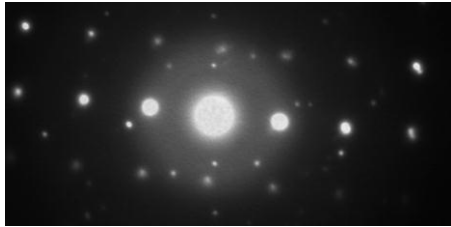
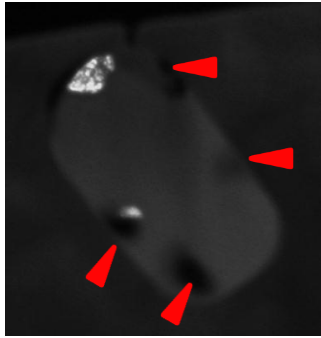


Figure 4. Kawakami et al

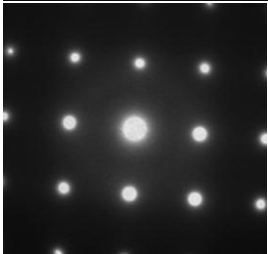
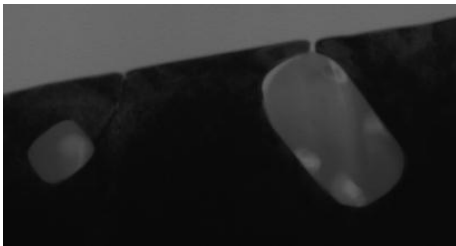


Kawakami et al Fig. 5 (full page width)

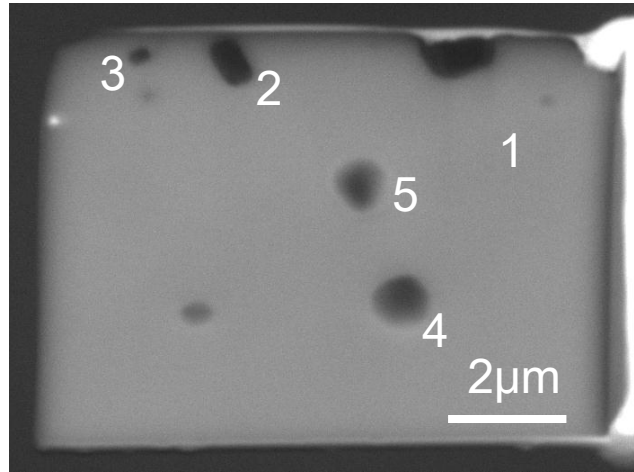
inclusion 2: Kfs + glass



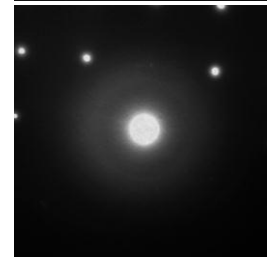
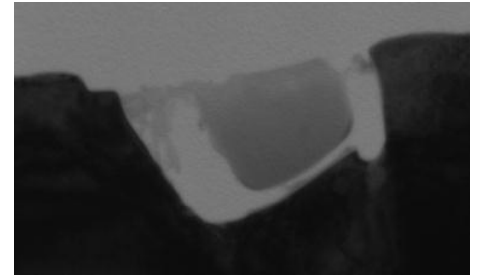
inclusion 3: glass (K,Al,Si-rich)



Sample G6



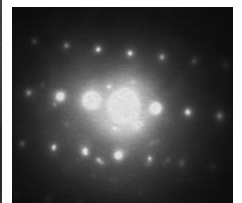
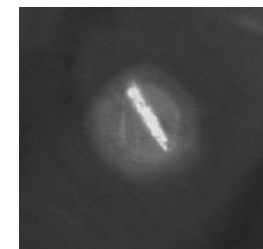
inclusion 1: glass (Si-rich)



inclusion 5: glass



inclusion 4: crystal



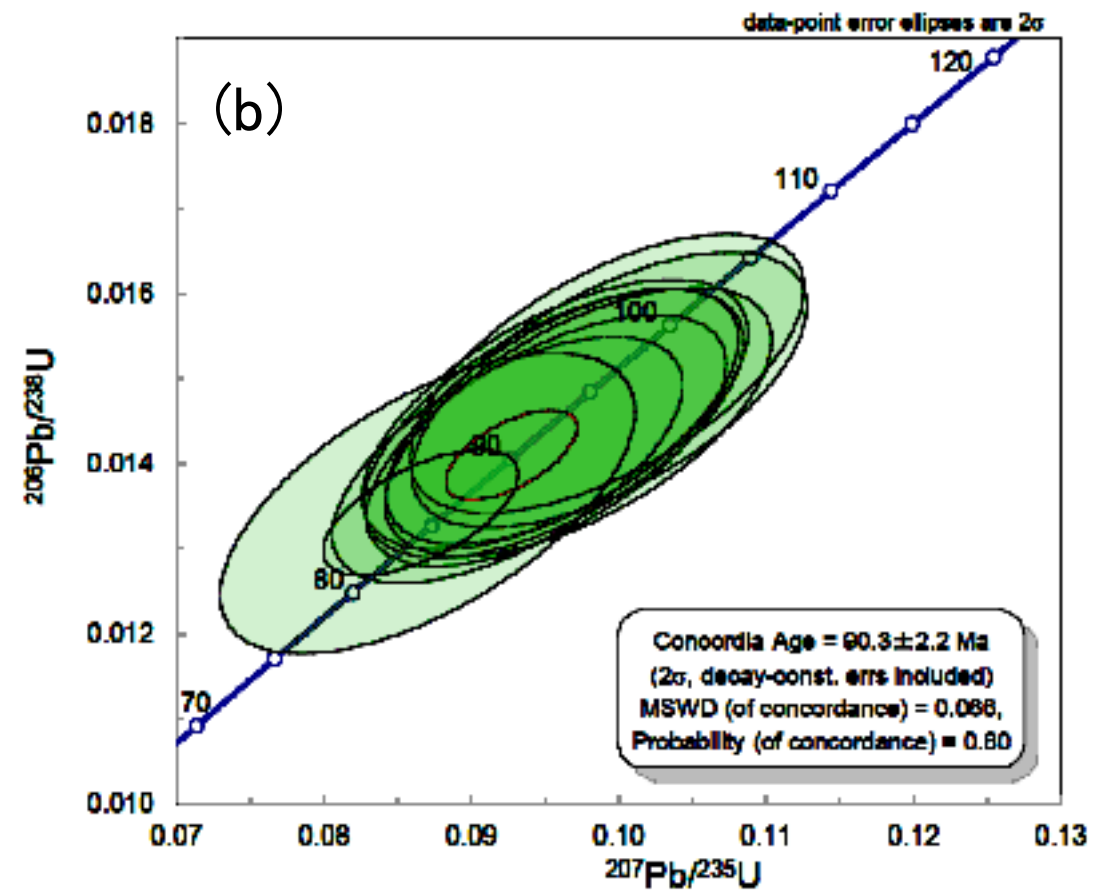
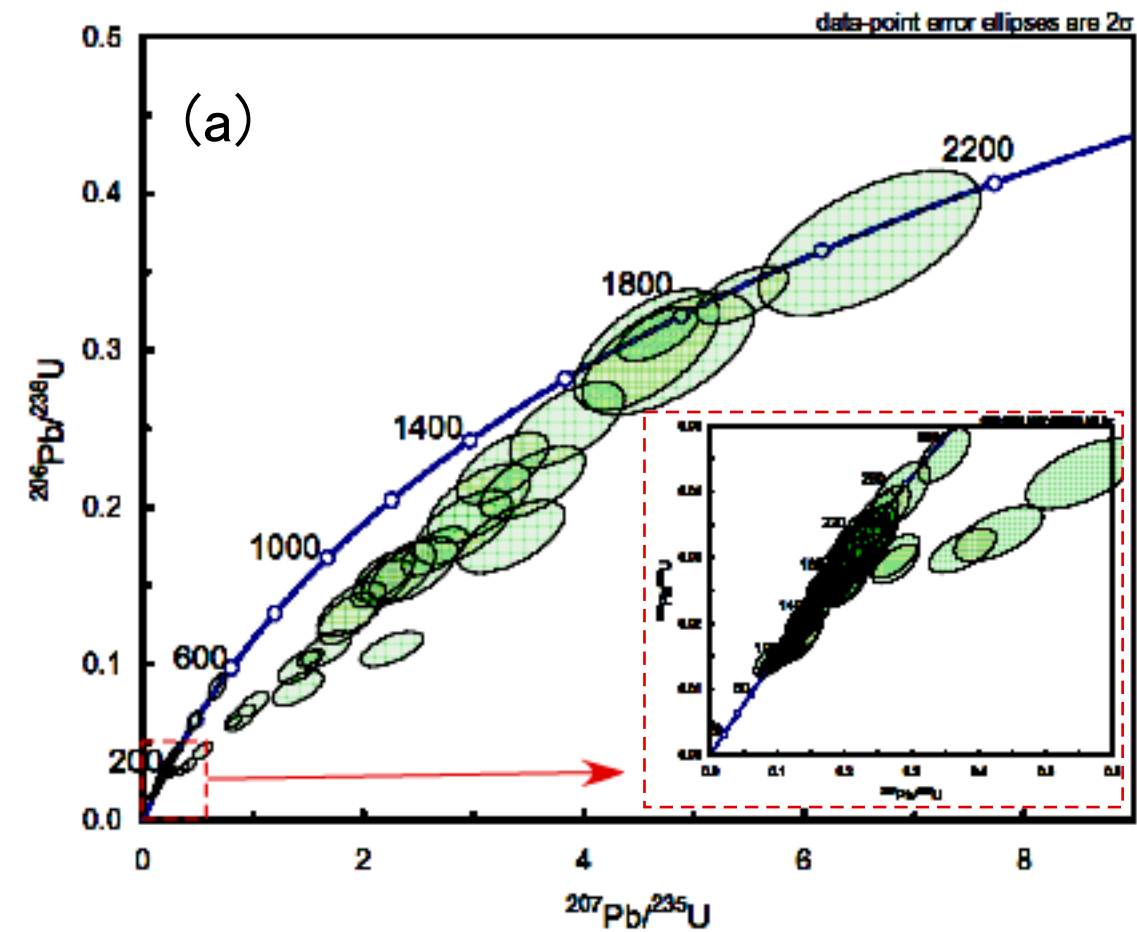
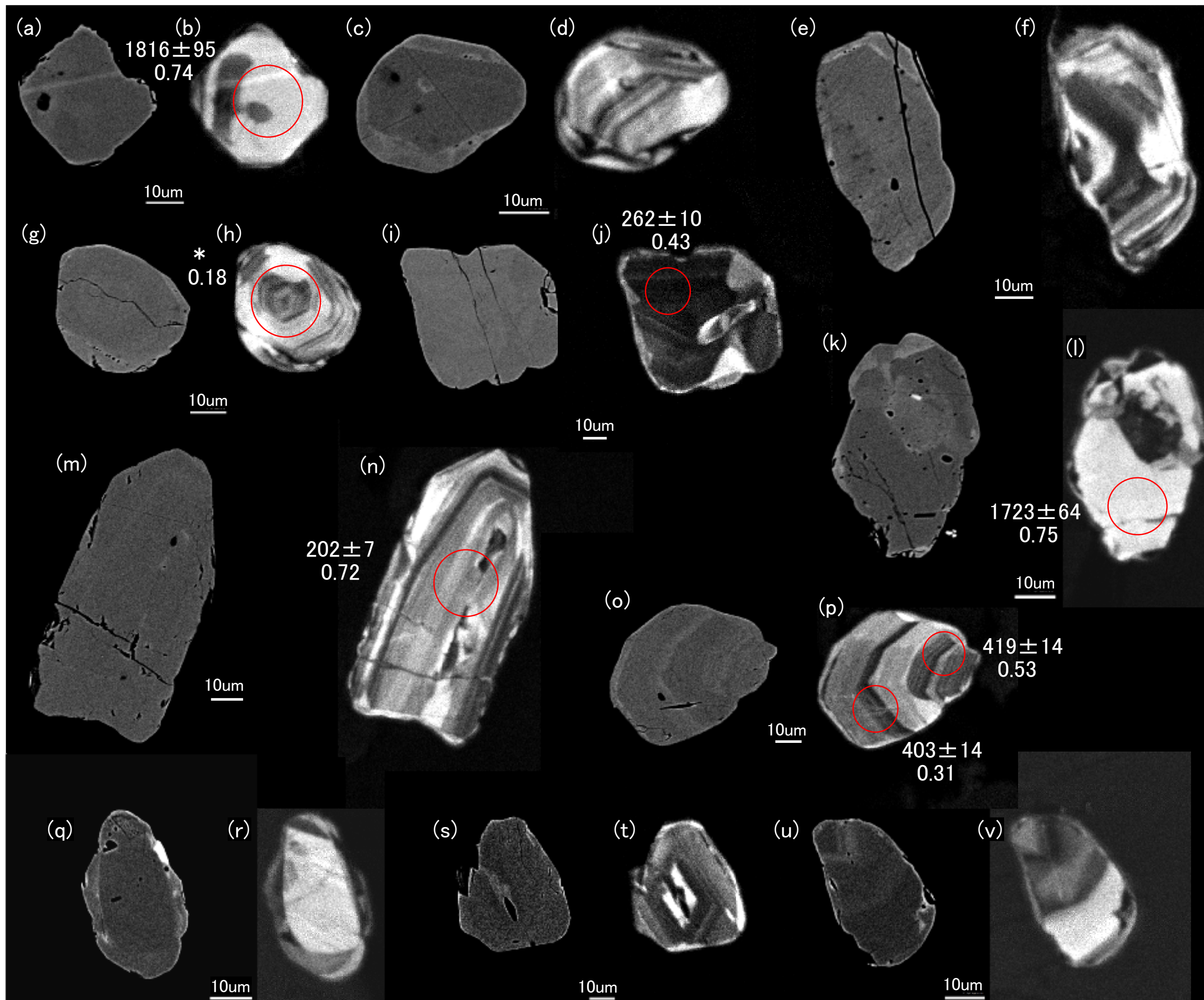
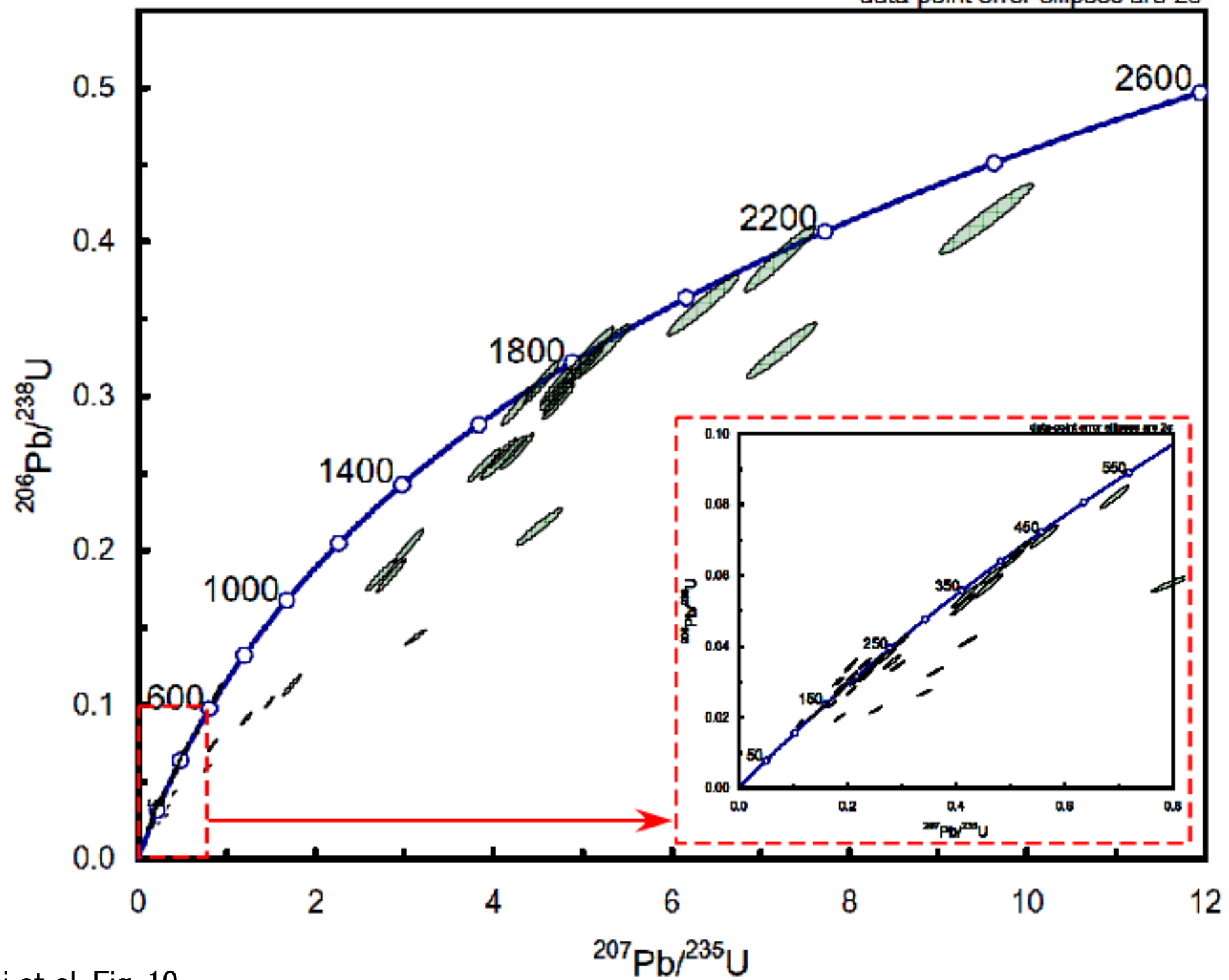


Figure 7 Kawakami et al.



Kawakami et al Fig. 8

data-point error ellipses are 2σ



Kawakami et al. Fig. 10

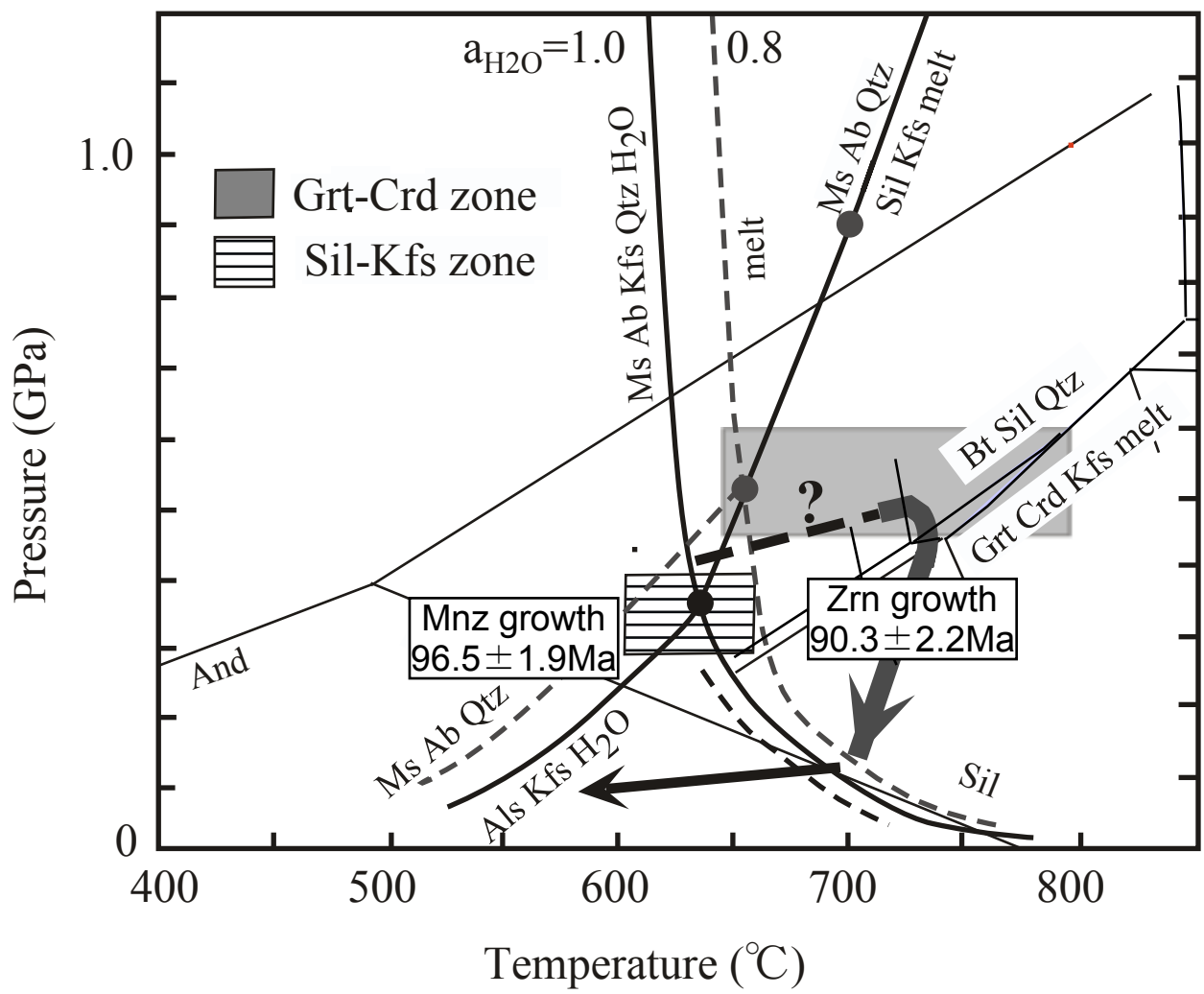


Fig. 11 Kawakami et al.

sample	location in the Grt-Crd zone	rock type	dark-CL annulus with inclusions	mineral assemblage (+Pl+Kfs+Qtz± retrograde Ms)	LA-ICP-MS Zrn dating	modal amount of Zrn>20µm (vol%)	modal amount of Zrn>20µm (vol%) rectangle	trace element concentration (ppm)								
								Cr	Ni	Ba	Rb	Nb	Pb	Sr	Zr	Y
AN16	north	psammitic schist	scarce	Bt	○	-	-	33	24	1266	104	8	27	234	313	20
AN24	north	pelitic schist	scarce	Bt+Crd(?)	○	0.013	0.016	49	24	1312	111	10	25	257	193	21
AN32	north	psammitic schist	scarce	Bt	○	0.013	0.016	29	21	384	91	6	18	214	119	11
AN28	middle	metatexite	common	Bt+Grt+Crd	-	-	-	45	29	510	64	9	9	108	105	15
AN02	middle	metatexite	common	Bt+Grt+Sil+Tur	-	0.0002	0.0002	48	47	677	128	9	31	112	170	29
AN06	middle	metatexite	common	Bt+Crd+Tur	-	-	-	56	48	962	192	10	30	281	249	25
AN07a	middle	metatexite	common	Bt+Grt+Tur	-	0.003	0.003	50	24	505	116	10	28	228	182	28
AN09	middle	metatexite	scarce	Bt+Grt (+Sil inc)	-	-	-	46	35	766	112	10	20	113	195	28
AN11	middle	metatexite	common	Bt+Grt	-	-	-	72	44	179	105	6	16	190	131	27
AN38	middle	metatexite	common	Bt+Grt+Crd	-	-	-	34	26	225	84	7	16	145	177	37
AN40	middle	metatexite	common	Bt+Grt+Crd+Tur	-	-	-	125	54	378	101	8	20	226	176	37
AN47	middle	metatexite	common	Bt+Grt+Crd (+Sil inc)	○	0.009	0.011	62	28	421	130	8	17	159	172	24
AN44	middle	metatexite	common	Bt+Grt+Crd+Sil	○	0.004	0.005	66	25	253	108	12	18	129	257	45
AN52	middle	metatexite	common	Bt+Grt	○	0.004	0.005	52	30	249	85	9	22	285	157	29
AN27	middle	metatexite	common	Bt+Grt+Crd+Sil	○	-	-	75	48	860	206	16	27	147	177	31
Y49B	south	metatexite	common	Bt+Grt+Crd+Sil	-	-	-	-	-	-	-	-	-	-	-	-
Y32A	south	diatexite	common	Bt+Crd+Sil	○	0.014	0.018	71	29	353	130	17	20	229	253	27
Y25	south	diatexite	common	Bt+Crd+Sil	○	0.011	0.013	73	40	589	167	19	23	209	193	22
G6	south	diatexite	common	Bt	○	0.008	0.010	109	47	258	96	14	21	232	211	17
G11	south	diatexite	rare	Bt+Grt+Sil	-	0.003	0.004	34	27	428	103	18	18	128	194	43

Table 1 Kawakami et al.

Nu AttoM single collector ICP-MS

RF power	1350 W
Cooling gas flow rate	13 l/min
Auxiliary gas flow rate	0.9 l/min
Detection system	Mixed attenuation-multiple ion counting
IC dead time	18 ns

NWR193 excimer laser system

ATLEX-SI ArF excimer laser	
Wavelength	193 nm
Pulse energy	7.0 mJ
Pulse width	4-6 ns
Energy density/ Fluence	1.60-2.23 J /cm ²
Repetition rate	6 Hz
Spot diameter	20 µm
Helium carrier gas flow rate	1.00 l/min
Argon make-up gas flow rate	1.05 l/min
Signal smoothing device	with
Number of laser shots	100 shots

Measured isotope	Dwell time		Attenuation
	Sample	Gas blank	
²⁰² Hg	1300 ms	2000 ms	Off
²⁰⁴ Pb	1300 ms	2000 ms	Off
²⁰⁶ Pb	1300 ms	2000 ms	Off
²⁰⁷ Pb	1300 ms	2000 ms	Off
²⁰⁸ Pb	1300 ms	2000 ms	Off
²³² Th	1300 ms	2000 ms	Off
²³⁸ U	1300 ms	2000 ms	On or Off
Data acquired time	11 sec	150 sec	

Kawakami et al. Table 2

7th July 2011, Department of Geology and Mineralogy, Kyoto University													Ages (Ma)			U-Pb discordance (%)	
Grain number	²⁰⁴ Pb (cps)	²⁰² Hg (cps)	U (ppm)	Th (ppm)	Th/U	²⁰⁴ Pb/ ²⁰⁶ Pb	²⁰⁶ Pb/ ²³⁸ U	±2SD	²⁰⁷ Pb/ ²³⁵ U	±2SD	²⁰⁷ Pb/ ²⁰⁶ Pb	±2SD	²⁰⁶ Pb/ ²³⁸ U age	±2SD	²⁰⁷ Pb/ ²³⁵ U age		±2SD
G6-15	1756	7487	660	3.1	0.005	0.0537	0.0134	0.0006	0.0866	0.0054	0.0465	0.0019	86.0	3.9	84.3	5.1	-2.0
G6-29	1783	7571	747	13.0	0.017	0.0538	0.0145	0.0013	0.0973	0.0107	0.0485	0.0019	92.8	8.2	94.3	9.9	1.6
G6-30	1720	7722	617	5.5	0.009	0.0538	0.0149	0.0013	0.0994	0.0110	0.0483	0.0019	95.2	8.4	96.2	10.1	1.1
G6-31	1785	7514	934	4.1	0.004	0.0538	0.0151	0.0013	0.0993	0.0109	0.0476	0.002	96.4	8.5	96.1	10.1	-0.4
G6-31r	1790	7616	1005	21.7	0.022	0.0538	0.0145	0.0013	0.0956	0.0105	0.0477	0.002	92.7	8.2	92.7	9.8	0.0
G6-34r	1797	7601	860	3.8	0.004	0.0538	0.0146	0.0013	0.0957	0.0107	0.0472	0.002	93.3	8.3	92.8	9.9	-0.6
G6-38r	1742	7701	583	3.4	0.006	0.0538	0.0143	0.0012	0.0951	0.0100	0.0482	0.0020	91.4	7.7	92.3	9.3	0.9
G6-40r	1848	7855	698	10.0	0.014	0.0537	0.0141	0.0012	0.0925	0.0097	0.0476	0.0020	90.0	7.5	89.8	9.0	-0.2
Y32-17	1852	7781	616	6.0	0.010	0.0538	0.0146	0.0012	0.0962	0.0098	0.0477	0.0026	93.2	7.8	93.3	9.1	0.1
Y32-38	1843	8050	430	4.0	0.009	0.0537	0.0135	0.0014	0.0871	0.0115	0.0471	0.002	86.7	9.2	84.8	10.7	-2.3

Table 3 Kawakami et al.